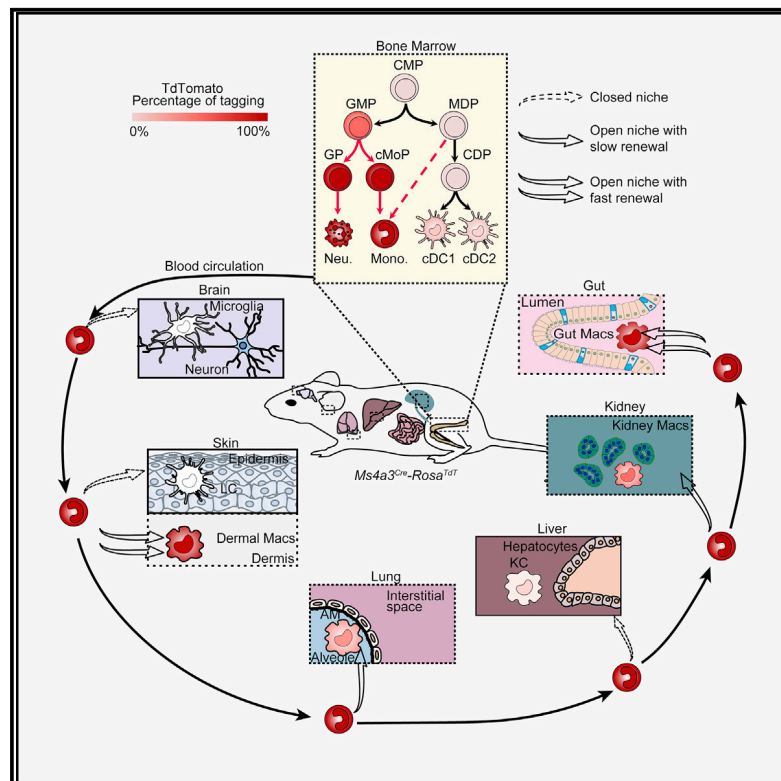


Fate Mapping via *Ms4a3*-Expression History Traces Monocyte-Derived Cells

Graphical Abstract



Authors

Zhaoyuan Liu, Yaqi Gu,
Svetoslav Chakarov, ..., Zhiduo Liu,
Bing Su, Florent Ginhoux

Correspondence

bingsu@sjtu.edu.cn (B.S.),
florent_ginhoux@immunol.a-star.edu.
sg (F.G.)

In Brief

A fate-mapping model provides insights into the ontogeny of specific monocyte populations and their contributions to the tissue-resident macrophage pools during homeostasis and inflammation.

Highlights

- *Ms4a3* is specifically and transiently expressed by GMPs in the bone marrow
- MDPs do not arise from GMPs and do not give rise to cMoPs
- *Ms4a3*-based models specifically and efficiently fate map monocytes and granulocytes
- Distinguish monocyte- versus embryonic-derived RTMs in steady state and inflammation



Fate Mapping via *Ms4a3*-Expression History Traces Monocyte-Derived Cells

Zhaoyuan Liu,¹ Yaqi Gu,¹ Svetoslav Chakarov,² Camille Bleriot,² Immanuel Kwok,² Xin Chen,¹ Amanda Shin,¹ Weijie Huang,¹ Regine J. Dress,² Charles-Antoine Dutertre,² Andreas Schlitzer,³ Jinmiao Chen,² Lai Guan Ng,² Honglin Wang,¹ Zhiduo Liu,¹ Bing Su,^{1,4,*} and Florent Ginhoux^{1,2,5,6,*}

¹Shanghai Institute of Immunology, Department of Immunology and Microbiology, Shanghai Jiao Tong University School of Medicine, Shanghai 200025, China

²Singapore Immunology Network, Agency for Science, Technology and Research, Singapore 138648, Singapore

³Myeloid Cell Biology, LIMES-Institute, University of Bonn, 53115 Bonn, Germany

⁴Key Laboratory of Cell Differentiation and Apoptosis of Chinese Ministry of Education, Shanghai Jiao Tong University School of Medicine, Shanghai 200025, China

⁵Translational Immunology Institute, SingHealth Duke-NUS Academic Medical Centre, Singapore, Singapore

⁶Lead Contact

*Correspondence: bing-su@sjtu.edu.cn (B.S.), florent_ginhoux@immunol.a-star.edu.sg (F.G.)

<https://doi.org/10.1016/j.cell.2019.08.009>

SUMMARY

Most tissue-resident macrophage (RTM) populations are seeded by waves of embryonic hematopoiesis and are self-maintained independently of a bone marrow contribution during adulthood. A proportion of RTMs, however, is constantly replaced by blood monocytes, and their functions compared to embryonic RTMs remain unclear. The kinetics and extent of the contribution of circulating monocytes to RTM replacement during homeostasis, inflammation, and disease are highly debated. Here, we identified *Ms4a3* as a specific gene expressed by granulocyte-monocyte progenitors (GMPs) and subsequently generated *Ms4a3^{TdT}* reporter, *Ms4a3^{Cre}*, and *Ms4a3^{CreERT2}* fate-mapping models. These models traced efficiently monocytes and granulocytes, but no lymphocytes or tissue dendritic cells. Using these models, we precisely quantified the contribution of monocytes to the RTM pool during homeostasis and inflammation. The unambiguous identification of monocyte-derived cells will permit future studies of their function under any condition.

INTRODUCTION

Tissue-resident macrophages (RTMs) have vital roles in tissue homeostasis, inflammation, and remodeling (Ginhoux and Jung, 2014), but their origins and maintenance are debated. Macrophages were originally proposed to be derived from circulating monocytes (van Furth and Cohn, 1968), but recent studies have challenged this model, causing an important conceptual frameshift in the field (Ginhoux et al., 2010; Guilliams et al., 2013; Hashimoto et al., 2013; Hoeffel et al., 2012; Jenkins et al., 2011; Schulz et al., 2012; Yona et al., 2013) (reviewed in Ginhoux and Guilliams [2016]). Namely, these studies revealed that adult RTMs arise from successive waves of embryonic

and adult hematopoiesis (reviewed in Hoeffel and Ginhoux [2015]), and the extent of contribution and the kinetics of these waves to each RTM population is tissue specific (Ginhoux and Guilliams, 2016).

The exact contribution of adult definitive hematopoiesis to RTMs is an area of intense investigation. Using parabiosis and genetic fate-mapping approaches, Hashimoto et al. showed that some RTMs (such as lung alveolar macrophages [AMs], red pulp macrophages, and peritoneal macrophages) self-maintain locally throughout adult life with minimal contribution from circulating monocytes (Hashimoto et al., 2013). Others have shown that barrier tissues, such as the gut and dermis, have a notable monocyte contribution (Bain et al., 2014; Tamoutounour et al., 2013). Furthermore, bone marrow (BM)-derived monocytes can differentiate into arterial macrophages immediately after birth and locally self-renew from this point (Ensan et al., 2016), suggesting that this tissue is only temporarily “open” at birth but remains “closed” during adulthood. Adult tissues can thus be classified as (1) closed, with no steady-state monocyte recruitment (brain, epidermis, lung, and liver) and self-maintained throughout life, without or with only minimal contribution of blood monocytes; (2) open, with fast steady-state recruitment (gut and dermis); or (3) open, with slow steady-state recruitment (heart and pancreas) (Ginhoux and Guilliams, 2016).

The mechanisms behind these differential renewal patterns are not fully understood and may be controlled by the tissue-specific microenvironment, sex, and/or other factors. Bain et al. showed that peritoneal macrophage renewal follows a sexually dimorphic pattern, with more monocytes contributing to peritoneal macrophages in males than in females (Bain et al., 2016). The situation during inflammation is even more complicated, as partial RTM depletion occurs alongside inflammatory cell recruitment, including neutrophils and monocytes (Guilliams and Scott, 2017). These monocytes may potentially contribute to RTMs upon resolution of inflammation (Guilliams and Scott, 2017). During *Listeria monocytogenes* infection, liver-resident macrophages undergo necroptosis in conjunction with rapid monocyte infiltration to give rise to monocyte-derived Kupffer cells (KCs) (Blériot et al., 2015). In an opposite scenario,



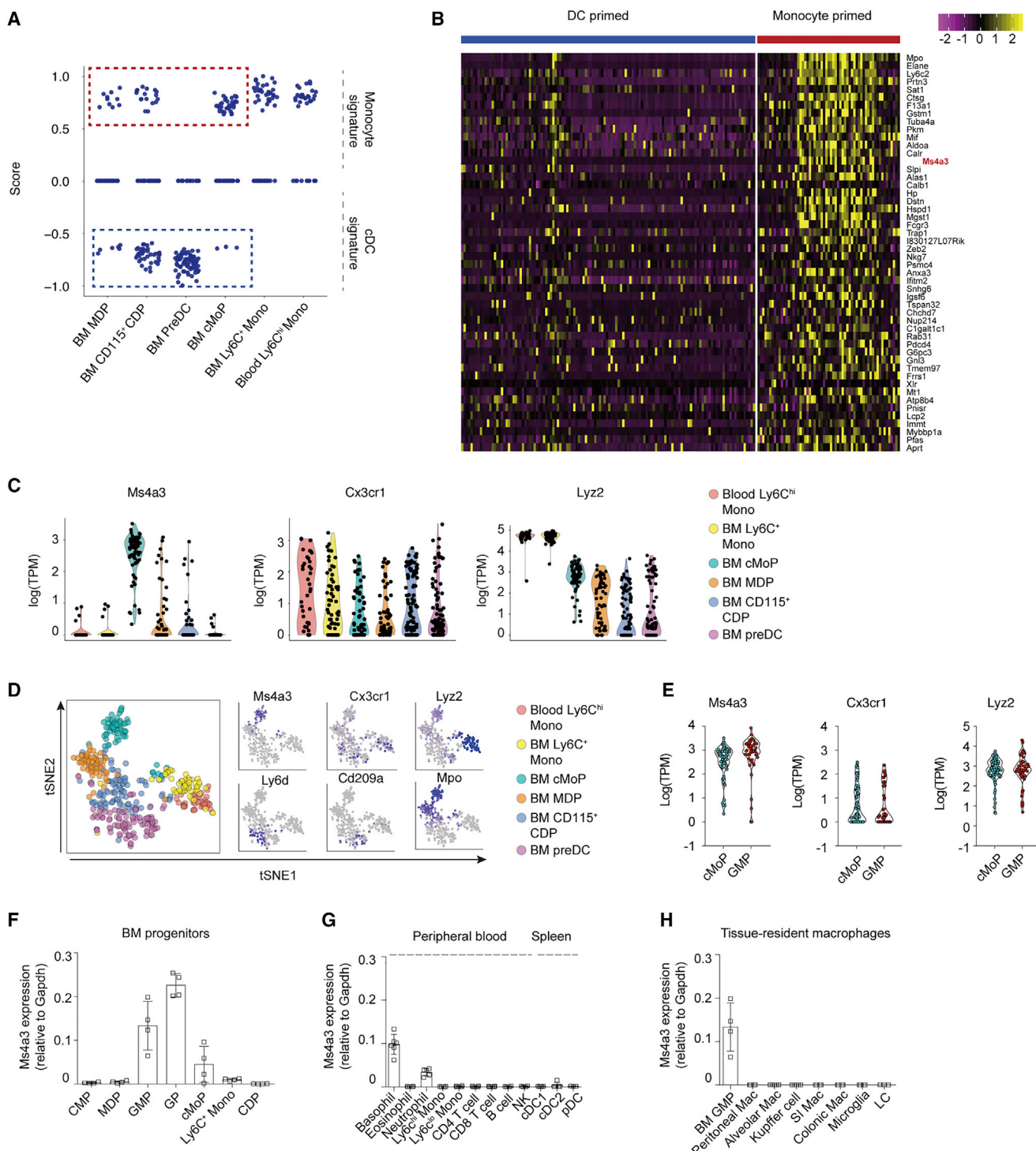


Figure 1. Ms4a3 Is Specifically Expressed by Monocyte-Committed Progenitors

(A) CMap analysis of individual single-cell populations showing enrichment for monocyte or DC signature genes. Cells with a positive CMap score were denoted as monocyte-primed cells; cells with a negative CMap score were denoted as DC-primed cells. Cells in the red rectangle (monocyte-committed cells) and blue rectangle (DC-committed cells) were used for DEG analysis.

(B) Heatmap of the top 50 DEGs upregulated in monocyte-primed cells (indicated by the red rectangle in A) than in DC-primed cells (indicated by the blue rectangle in A). Yellow, high expression; purple low expression.

(C) Violin plot of Ms4a3, Cx3cr1, and Lyz2 expression in indicated populations. y axis represents the TPM (transcript per million reads) of the gene in each single cell.

(legend continued on next page)

during type 2 inflammation induced by *Litomosoides sigmodontis* infection, it is local macrophage proliferation rather than inflammatory cell recruitment that controls macrophage expansion in C57BL/6 mice (Jenkins et al., 2011). These observations suggest that the developmental stage, and tissue-specific and inflammation-specific conditions, controls the origins of RTMs under steady state and during inflammation. There is thus a need to precisely identify the origins of RTMs under any condition.

Monocyte fate-mapping models, including *Cx3cr1^{Cre}* or *Cx3cr1^{CreERT2}* (Yona et al., 2013) and *LyzM^{Cre}* (Clausen et al., 1999) are not fully accurate, labeling either dendritic cells (DCs) or RTMs respectively. Here, we aimed to develop a new fate-mapping mouse model specific for monocyte progenitors that could precisely measure the contribution of monocytes to RTMs under any condition and discern monocytes from DCs. The earliest monopotent BM progenitors giving rise to monocytes are common monocyte progenitors (cMoPs) (Hettinger et al., 2013), although commitment to monocytes occurs earlier as shown by single-cell mRNA sequencing (scRNA-seq) (Giladi et al., 2018; Paul et al., 2015). cMoPs are proposed to arise from the hierarchical model of common myeloid progenitor (CMP) → granulocyte-monocyte progenitor (GMP) → monocyte-dendritic cell progenitor (MDP) → cMoP (Ginhoux and Jung, 2014; Williams et al., 2018; Terry and Miller, 2014). We thus performed single-cell profiling of progenitor cells and subsequent bioinformatic analysis to identify candidate genes expressed solely by monocyte-committed progenitors to track their progeny. We identified the membrane-spanning 4-domains, subfamily A, member 3 (*Ms4a3*) as a specific gene to faithfully track GMPs and cMoPs but not MDPs and their DC progeny. We generated *Ms4a3^{TdT}* reporter, *Ms4a3^{Cre}-Rosa^{TdT}* fate-mapper, and *Ms4a3^{CreERT2}-Rosa^{TdT}*-inducible fate-mapper models to specifically dissect monocyte-differentiation pathways as well as follow monocytes and their progenies according to different tissues, ages, and sex and to quantify their contribution to the RTM pool during homeostasis and inflammation.

RESULTS

Ms4a3 Is Specifically Expressed by Monocyte-Committed Progenitors

We first aimed to identify a suitable gene to generate a *Cre*-recombinase-based monocyte fate-mapping model, by profiling the genes expressed in BM cMoPs and monocytes, but not in DC progenitors, such as common dendritic cell progenitors (CDPs), circulating DC precursors (pre-DCs) (to distinguish monocytes versus DCs), or differentiated macrophages (to distinguish monocyte contribution versus intrinsic expression in macrophages). MDPs have bi-potential, giving rise to both

DCs and monocytes (Auffray et al., 2009). We hypothesized that within the MDP population, MDPs that are committed to the monocyte lineage co-exist with MDPs committed to the DC lineage. We thus aimed to find a gene that is uniquely expressed in MDPs that are committed to the monocyte lineage.

We performed a single-cell transcriptomic analysis of monocyte and DC progenitors by scRNA-seq using the C1 Fluidigm platform (Figure S1A for workflow). We sorted BM cMoPs (Lin⁻CD117⁺CD115⁺CD135⁻Ly6C⁺), BM Ly6C⁺ monocytes (Lin⁻CD117⁻CD115⁺CD135⁻Ly6C⁺), and blood Ly6C^{hi} monocytes (CD115⁺CD11b⁺Ly6C^{hi}) from wild-type (WT) C57BL/6 mice by fluorescence-activated cell sorting (FACS) (Figures S1B and S1C for gating strategy) and generated transcriptional profiles for each individual cell (n = 38 for blood Ly6C^{hi} monocytes, n = 66 for BM cMoPs, n = 57 for BM Ly6C⁺ monocytes). We referred to our previously published dataset for MDPs (Lin⁻CD11c⁻MHCII⁻CD135⁺CD115⁺CD117^{hi}), CDPs (Lin⁻CD11c⁻MHCII⁻CD135⁺CD115⁺CD117^{int}), and pre-DCs (Lin⁻CD11c⁺MHCII⁻CD135⁺CD172a⁻) (Schlitzer et al., 2015). To identify putative monocyte-primed versus DC lineage-primed cells within these precursors, we compared the transcriptomic signatures of each single cell to DC versus monocyte- and/or macrophage-specific signatures (Schlitzer et al., 2015) using Connectivity Map (CMap) analysis (Lamb et al., 2006) (Figure 1A; see STAR Methods for bioinformatics analysis details). Here, we identified within the whole MDP stage single MDPs committed to the monocytic lineage versus the DC lineage (Figure 1A).

As expected, progenitor populations downstream of the MDP stage mostly exhibited either monocyte (cMoPs and monocytes) or DC (CDPs and pre-DCs) commitment. We identified the differentially expressed genes (DEGs) (see STAR Methods for bioinformatics analysis details) between monocyte-primed progenitors (red rectangle in Figure 1A) versus DC-primed progenitors (blue rectangle in Figure 1A), and selected the top 50 up-regulated genes in monocyte-primed progenitors compared to DC-primed progenitors (Figure 1B). After screening the expression profiles of these 50 genes in our scRNA-seq data and the ImmGen (Heng et al., 2008) and bioGPS databases (Wu et al., 2009), we identified *Ms4a3* as a potential candidate gene because of its high and specific expression profile in BM monocyte progenitors (Figures 1B, 1C, and S1D). *Ms4a3* is a member of the membrane-spanning 4A gene family and is closely related to CD20 and the beta-subunit of the high-affinity immunoglobulin E (IgE) receptor (FcεRIβ) (Hulett et al., 2001). Using the ImmGen database, we found that *Ms4a3* is highly expressed in BM GMPs, lowly expressed in MDPs (Figure S1E), and not expressed in DCs or various RTMs (Figure S1F). Exploring the bioGPS database, we found *Ms4a3* to be only expressed in the BM, predominantly by GMPs (Figure S1G). With our single-cell sequencing data, we visualized *Ms4a3* expression overlaid on

(D) tSNE plot of cell populations and the *Ms4a3*, *Cx3cr1*, and *Lyz2* expression profiles. Blue, high expression; gray, low expression.

(E) Violin plots of *Ms4a3*, *Cx3cr1*, and *Lyz2* expression in BM GMPs (Lin⁻Sca-1⁻CD117⁺CD16/32^{hi}CD34⁺) and BM cMoPs. y axis represents the TPM of *Ms4a3* in each single cell.

(F) qRT-PCR analysis of *Ms4a3* expression in BM progenitors (n = 4). The expression was normalized to *Gapdh* (2^{-delta Ct}). Error bars, SEM.

(G) qRT-PCR analysis of *Ms4a3* expression in the indicated cell types in the peripheral blood and spleen (n = 4–6). Error bars, SEM.

(H) qRT-PCR analysis of *Ms4a3* expression in RTMs in different organs (n = 3–4). Error bars, SEM.

See also Figures S1 and S2.

the t-distributed stochastic neighbor embedding (tSNE) plot (Figure 1D). In this analysis, *Ms4a3* was highly expressed in cMoPs but not in CDPs, suggesting its potential utility to distinguish monocytes from DCs in a fate-mapping approach (Figures 1C and 1D). We also compared the expression of *Ms4a3* with *Cx3cr1* and *Lyz2*, genes used to previously make monocyte fate-mapping models. In contrast to *Ms4a3*, which was only expressed in cMoPs but not in terminally differentiated blood $Ly6C^{hi}$ monocytes, *Lyz2* was expressed at a higher level in terminally differentiated $Ly6C^{hi}$ monocytes than in cMoPs and was also expressed by pre-DCs, while *Cx3cr1* was expressed by both monocyte-primed cells and DC-primed cells (Figures 1C and 1D). We also verified at the single-cell level that *Ms4a3* was expressed by GMPs (single-cell dataset published in Dress et al. [2019]) (Figure 1E). To confirm these data, we sorted BM CMPs, GMPs, granulocyte progenitors (GPs), cMoPs, MDPs, CDPs, and $Ly6C^+$ monocytes (Figure S2A for gating strategy) and profiled *Ms4a3* expression by quantitative real-time polymerase chain reaction (qRT-PCR). Consistent to the scRNA-seq data and the expression data from the ImmGen and bioGPS databases, we detected high *Ms4a3* expression in BM GMPs and cMoPs (Figure 1F). In summary, our single-cell sequencing data, qRT-PCR data, and expression data from public databases suggest that *Ms4a3* is highly and specifically expressed in GMPs, GPs, and cMoPs and might be more suitable to specifically fate map monocytes than *Cx3cr1* and *Lyz2*.

***Ms4a3* Is Not Expressed by RTMs or DCs**

Here, we hypothesized that *Ms4a3* is a suitable target gene for building a monocyte fate mapper that could precisely measure the contribution of monocytes to RTMs on the condition that it is not expressed in mature RTMs or DCs. We first verified that *Ms4a3* was not expressed by RTMs or DCs in the ImmGen and bioGPS databases (Figures S1F and S1G). To confirm these data, we sorted cell populations of interest from various tissues and profiled *Ms4a3* expression by qRT-PCR (Figures S2B–S2D for gating strategy). *Ms4a3* was expressed in basophils and neutrophils in the blood but not expressed in lymphocytes (T cells, B cells, and natural killer [NK] cells), mature monocytes, eosinophils, or splenic DCs (conventional dendritic cell 1 [cDC1], cDC2, and plasmacytoid DCs [pDCs]) (Figure 1G). We next measured *Ms4a3* expression in several RTM populations and detected no notable expression in peritoneal macrophages, lung AMs, liver KCs, gut macrophages, microglia, or Langerhans cells (LCs) (Figures 1H and S2E–S2J for gating strategy).

Ms4a3 is a membrane-associated protein located in the perinuclear area but not at the cell surface (Donato et al., 2002), and no antibodies for mouse *Ms4a3* are commercially available, limiting expression detection by flow cytometry. To monitor the expression of *Ms4a3* at the single-cell level, we developed a *Ms4a3* reporter mouse by inserting an *Ires-tdTomato* sequence downstream of the *Ms4a3* stop codon (denoted as *Ms4a3^{TdT}* mice hereafter) (Figure S3A). In this model, we expected tdTomato to be expressed as a faithful reporter in *Ms4a3*-expressing cells. Indeed, in the BM of *Ms4a3^{TdT}* mice, the earliest tdTomato signal appeared in GMPs and was detectable in cMoPs and monocytes (albeit to a lesser extent) (Figure 2A), which is in agreement with our qRT-PCR profiling (Figure 1F).

Furthermore, we confirmed high tdTomato protein expression levels in peripheral blood basophils and neutrophils and a low level in monocytes, likely reflecting the residual expression of the tdTomato protein initiated in the BM and no expression in lymphoid lineages (Figures 2B and 2C), splenic cDC1, cDC2, or pDCs (Figure 2D). Profiling of tdTomato mRNA by qRT-PCR led to a similar profile with high mRNA levels in BM GMPs and cMoPs but very low levels in blood monocytes (Figure 2E). We compared these results to the commonly used monocyte reporter model *Cx3cr1^{gfp}* mice (Jung et al., 2000). BM cMoPs and monocytes expressed the GFP reporter, but also MDPs and CDPs (Figure S3B), consistent with a previous report (Yona et al., 2013). In the blood, monocytes expressed a high level of *Cx3cr1*-GFP, besides basophils and some NK cells (Figures S3C and S3D). In the spleen, some DCs were positive for *Cx3cr1*-GFP (Figure S3E) while negative for *Ms4a3*-tdTomato in the *Ms4a3^{TdT}* model (Figure 2D). In a *Ms4a3^{TdT};Cx3cr1^{gfp}* model, the overlap between tdTomato and GFP could only be detected in monocytes and some basophils in the peripheral blood (Figure 2F). From $Ly6C^{hi}$ to $Ly6C^{lo}$ monocytes, the expression of GFP increased while the tdTomato expression decreased (Figure 2G). These populations can be clearly identified based on the differential expression of *Cx3cr1*-GFP and *Ms4a3*-tdTomato (Figure S3F). These data support the concept that *Ms4a3*-based fate-mapping models would help to distinguish monocytes from the cells of the DC lineage.

We next analyzed tdTomato expression in several RTM populations (brain microglia, skin LCs, liver KCs, lung AMs, splenic macrophages, peritoneal macrophages, kidney macrophages, gut macrophages, and dermal macrophages) in young (8-week-old) and old (6-month-old) *Ms4a3^{TdT}* mice, and consistent with our qRT-PCR data (Figure 1G), we found that none of them expressed tdTomato (Figures S4A–S4I). We also analyzed the expression of the GFP reporter in RTMs of *Cx3cr1^{gfp}* mice, and consistent with a previous report (Yona et al., 2013), microglia, gut macrophages, and kidney macrophages express in steady state a high level of the reporter (Figures S4A–S4I), which limits the use of this model to distinguish embryonic macrophages from monocyte-derived macrophages. Collectively, these data suggest that *Ms4a3* is a specific marker for BM GMP and cMoP stages and may be suitable for labeling GMPs and their progenies, including monocytes.

***Ms4a3^{Cre}-Rosa^{TdT}* Model Specifically and Efficiently Fate Maps Granulocytes and Monocytes**

We next generated a *Ms4a3^{Cre}* fate-mapper mouse model by inserting an *Ires-Cre* cassette downstream of the *Ms4a3* stop codon (Figure S5A) and crossed this strain with the *Rosa26^{tdTomato}* reporter strain. In the resulting *Ms4a3^{Cre}-Rosa^{TdT}* model, Cre recombinase will delete the *Stop* signal adjacent to *tdTomato* in *Ms4a3*-expressing cells, resulting in irreversible and persistent tdTomato red fluorescent protein expression in *Ms4a3*-expressing cells and their progeny (Figure S5A). According to the BioGPS database, where *Ms4a3* is only expressed in the BM (Figure S1G), we predicted no tdTomato labeling in *Ms4a3^{Cre}-Rosa^{TdT}* non-hematopoietic cells. Indeed, we found no tdTomato labeling in non-hematopoietic $CD45^-$ cells in the brain, skin, liver, lung, kidney, pancreas, heart, salivary gland, colon, or small intestine. We did, however, observe ~60%

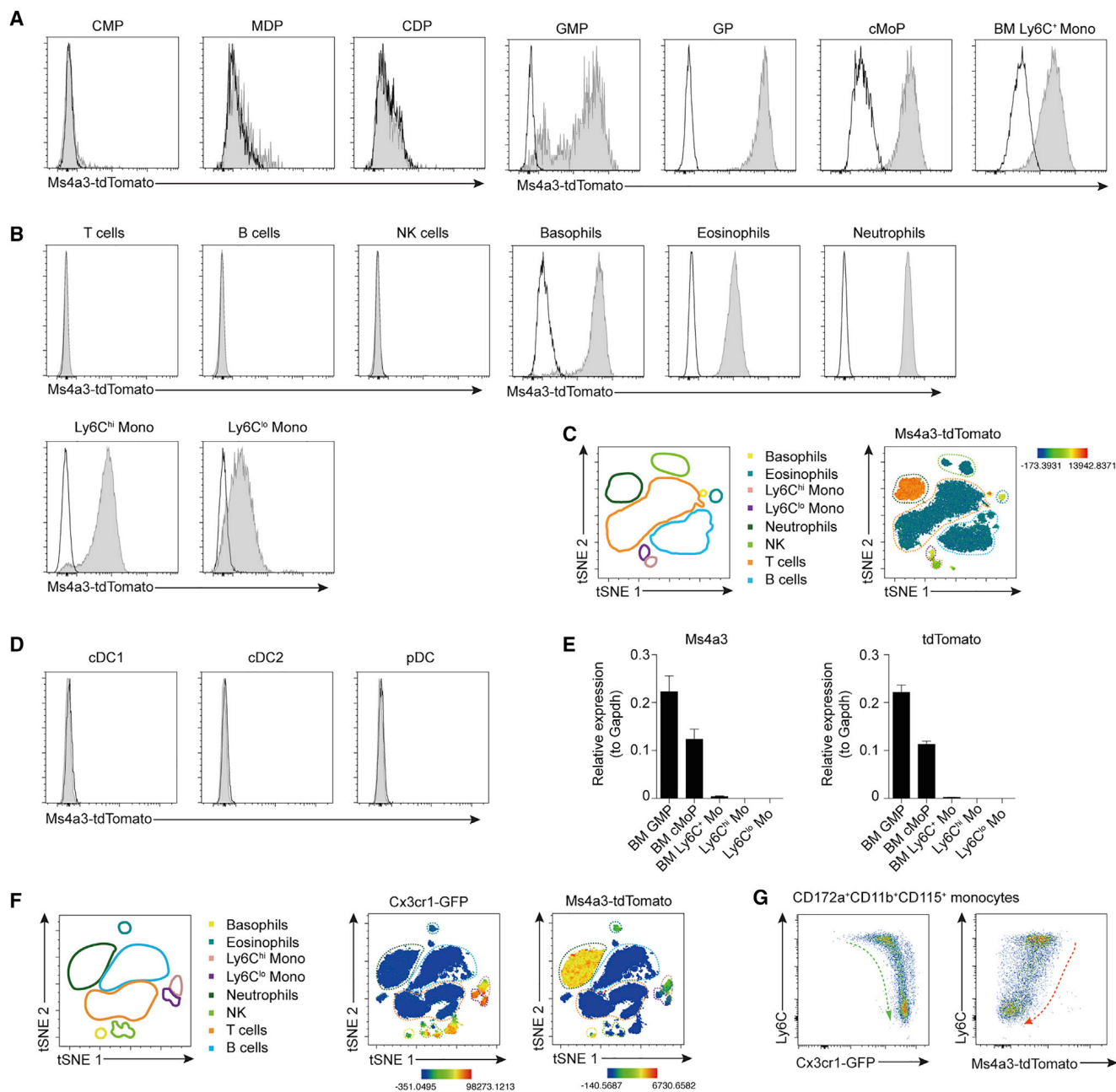


Figure 2. tdTomato Expression in *Ms4a3*^{TdT} Mice

(A) tdTomato expression in indicated progenitor cell types in the BM of *Ms4a3*^{TdT} (filled gray) and WT (open) mice.

(B) tdTomato expression in indicated cell types in the peripheral blood of *Ms4a3*^{TdT} mice (filled gray) and WT (open) mice.

(C) tSNE plot shows the intensity of tdTomato in peripheral blood cells. The color indicates the expression intensity of tdTomato: red, high expression; blue, low expression.

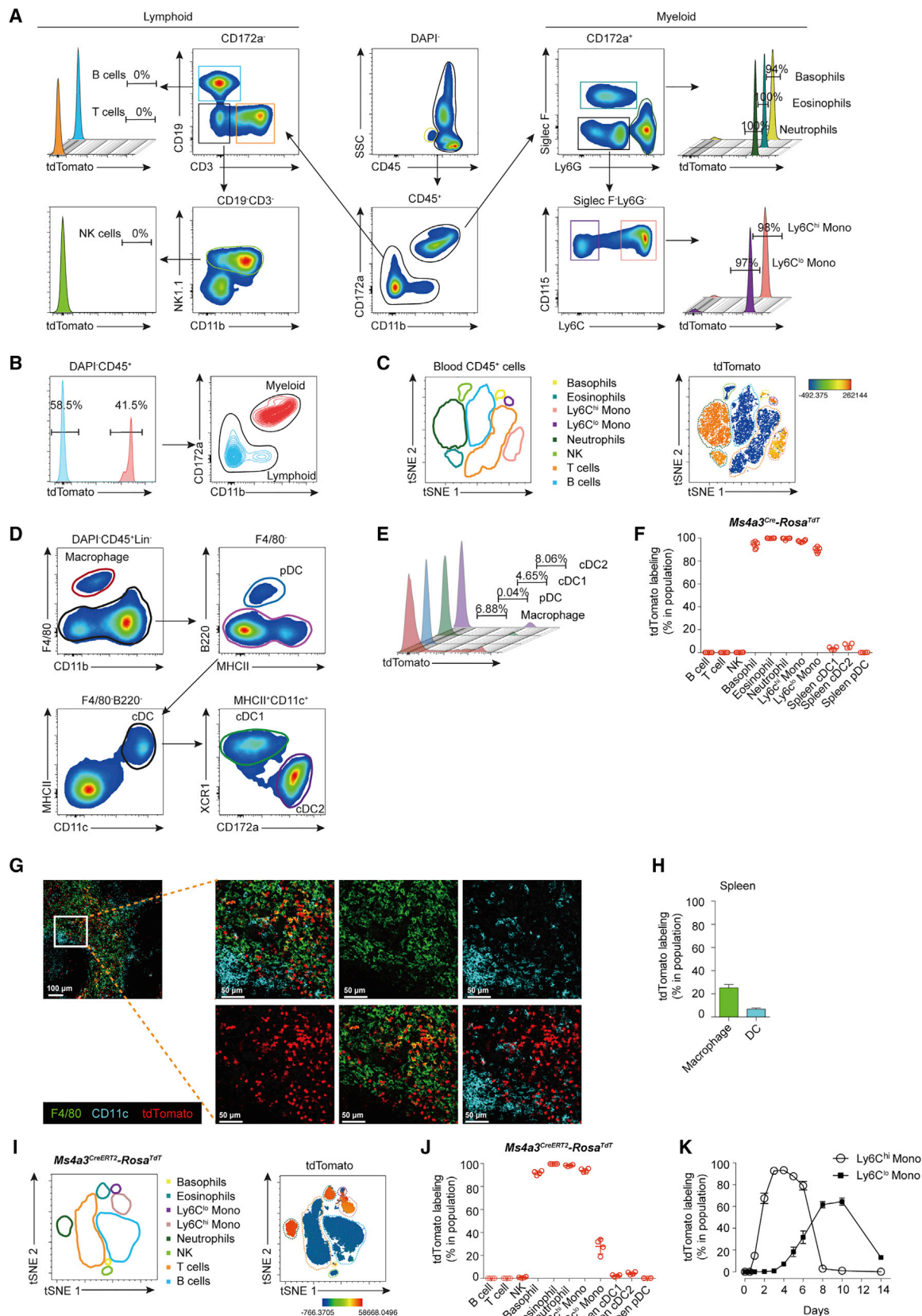
(D) tdTomato expression in splenic cDCs and pDCs in *Ms4a3*^{TdT} mice (filled gray) and WT (open) mice. Each experiment was repeated at least 3 times with 2–3 replicates, and a representative plot is shown.

(E) qRT-PCR analysis of *Ms4a3* and tdTomato expression in indicated populations ($n = 4$). Expression was normalized to *Gapdh* ($2^{-\Delta\Delta Ct}$). Error bars, SEM.

(F) tSNE plot shows the expression of Cx3cr1-GFP and *Ms4a3*-tdTomato in the peripheral blood of *Cx3cr1*^{GFP};*Ms4a3*^{TdT} mice. Red, high expression; blue, low expression.

(G) Flow plots show the expression of Cx3cr1-GFP and *Ms4a3*-tdTomato in monocytes, waterfall from Ly6C^{hi} to Ly6C^{lo}.

See also [Figures S3 and S4](#).



(legend on next page)

tdTomato labeling in CD45⁺ cells in the testicles (Figure S5B) and confirmed low tdTomato expression in sperm by microscopy (Figure S5C); we did not detect any tdTomato expression in adult testicles in *Ms4a3^{TdT}* reporter mice (Figure S5D). Going forward, to circumvent potential biases generated by germ-line recombination, we did not use *Ms4a3^{Cre}-Rosa^{TdT}* male mice as breeders.

We then analyzed tdTomato labeling in leukocyte lineages in the peripheral blood, spleen, and various tissues of our *Ms4a3^{Cre}-Rosa^{TdT}* model. As expected, lymphoid cells in the peripheral blood, including T cells (0.03% ± 0.001%), B cells (0.004% ± 0.001%), and NK cells (0.120% ± 0.027%), were not labeled, while neutrophils (99.9% ± 0.048%), basophils (94.1% ± 1.151%), eosinophils (99.5% ± 0.309%), Ly6C^{hi} monocytes (97.3% ± 0.320%) and Ly6C^{lo} monocytes (95.1% ± 0.530%) were highly labeled (Figures 3A and S5E). When performing a reverse analysis by first gating on tdTomato⁺ cells, almost all tdTomato⁺ cells were CD172a⁺CD11b⁺ myeloid cells (Figure 3B). tSNE analysis clearly showed that tdTomato⁺ cells were neutrophils, basophils, eosinophils, and monocytes (Figure 3C).

We then analyzed tdTomato labeling in splenic DCs. Here, we detected a low level of labeling in XCR1⁺ cDC1s (3.585% ± 0.652%) and CD172a⁺ cDC2s (6.000% ± 1.012%) and no labeling in MHCII^{int}B220⁺CD172a⁺ pDCs (0.075% ± 0.033%) (Figures 3D–3F). We confirmed these findings by microscopy, where we observed negligible overlap between tdTomato (red) and CD11c⁺ (cyan) cells (considered DCs) in the spleen (Figures 3G and 3H). Finally, we did a parallel comparison of *Ms4a3^{Cre}-Rosa^{TdT}* with *Cx3cr1^{Cre}-Rosa^{TdT}*. The latter mainly labels monocytes and DCs, but also with very high background labeling in lymphocytes and granulocytes (Figures S5F and S5G), while *Ms4a3^{Cre}-Rosa^{TdT}* only specifically labels monocytes and granulocytes. Taken together, the *Ms4a3^{Cre}-Rosa^{TdT}* mouse model permits faithful genetic marking of monocytes and granulocytes, but not DCs or lymphocytes.

***Ms4a3^{CreERT2}-Rosa^{TdT}* Model Specifically and Efficiently Fate Maps Granulocytes and Monocytes**

We also developed a tamoxifen-inducible model (named *Ms4a3^{CreERT2}*) by inserting an *Ires-CreERT2* cassette down-

stream of the *Ms4a3* stop codon and crossed this strain with the *Rosa26^{tdTomato}* reporter strain (Figure S5H). This conditional fate-mapping model contains a Cre recombinase fused to a mutant estrogen ligand-binding domain (CreERT2) that requires the estrogen antagonist tamoxifen for activity (Feil et al., 1997). Upon tamoxifen injection, *Ms4a3*-expressing cells will start to express the tdTomato reporter in an irreversible fashion, allowing us to fate map the contribution of GMPs in a time-controlled manner.

Ms4a3^{CreERT2}-Rosa^{TdT} mice were given tamoxifen for 4 successive days by intraperitoneal (i.p.) injection and analyzed on day 7 (Figure S5I). Consistent with *Ms4a3^{Cre}-Rosa^{TdT}* mice, neutrophils (99.6% ± 0.05%), eosinophils (91.8% ± 0.87%), basophils (98.3% ± 0.34%), and Ly6C^{hi} monocytes (94.0% ± 0.78%) were labeled (Figures 3I and 3J). However, Ly6C^{lo} monocytes were labeled with a lower percentage (27.9% ± 3.33%) (Figure 3J) and in a more delayed fashion than Ly6C^{hi} monocytes (Figure 3K), in agreement with the developmental relationship between these subsets, with Ly6C^{hi} monocytes giving rise to Ly6C^{lo} monocytes (Yona et al., 2013). A similar level of labeling was observed in Ly6C^{hi} monocytes from the *Cx3cr1^{CreERT2}* mice (91.4% ± 2.38%) (Figures S5J and S5K). In contrast, DCs (62.7% ± 1.01% for cDC1, 37.4% ± 1.47% for cDC2, and 67.0% ± 2.29% for pDC) were labeled in *Cx3cr1^{CreERT2}-Rosa^{TdT}* mice (Figure S5K) while not in *Ms4a3^{CreERT2}-Rosa^{TdT}* mice (2.20% ± 0.40% for cDC1, 4.35% ± 0.60% for cDC2, and 0.10% ± 0.04% for pDC) (Figure 3J). In summary, the *Ms4a3^{CreERT2}-Rosa^{TdT}* model permits the faithful genetic marking of monocytes and granulocytes but not DCs or lymphocytes.

***Ms4a3* Labels GMPs but Not MDPs in the BM**

Monocytes are proposed to arise from the hierarchical model of CMP → GMP → MDP → cMoP → monocyte (Ginhoux and Jung, 2014; Guilliams et al., 2018; Terry and Miller, 2014). However, this model has been recently challenged by Yanez et al., who proposed that MDPs arise directly from CMPs independently of GMPs and that GMPs and MDPs give rise to distinct monocytes via similar pathways through monocyte-committed progenitors (MP) and cMoPs, respectively (Yanez et al., 2017). To test this hypothesis and to explore at which stage monocytes

Figure 3. *Ms4a3^{Cre}-Rosa^{TdT}* Model Specifically and Efficiently Fate Maps Granulocytes and Monocytes

- (A) The gating strategy and tdTomato labeling of lymphoid and myeloid lineages in the peripheral blood of *Ms4a3^{Cre}-Rosa^{TdT}* mice.
 (B) tdTomato⁺ cells (red) and tdTomato⁻ cells (blue) in peripheral blood were overlaid onto CD172a versus CD11b plot.
 (C) tSNE analysis showing tdTomato expression across different cell types in CD45⁺ blood cells of *Ms4a3^{Cre}-Rosa^{TdT}* mice. Red, high expression; blue, low expression.
 (D) Gating strategy for splenic DCs and macrophages.
 (E) tdTomato labeling of splenic macrophages (CD45⁺Lin⁻F4/80⁺), pDC (Lin⁻B220⁺CD172a⁺), cDC1 (Lin⁻CD11c⁺MHCII⁺XCR1⁺), and cDC2 (Lin⁻CD11c⁺MHCII⁺CD172a⁺). Lin: CD3e, CD19, CD49b, and Ly6G.
 (F) tdTomato labeling in different lymphoid and myeloid lineages of *Ms4a3^{Cre}-Rosa^{TdT}* mice. The data are representative of 6–9 individual mice analyzed in two independent experiments. Error bars, SEM.
 (G) Confocal imaging of splenic F4/80⁺ macrophages (green), CD11c⁺ DCs (cyan), and tdTomato (red).
 (H) Relative numbers of tdTomato⁺ cells in F4/80⁺ macrophages and CD11c⁺ DCs from (G).
 (I) tSNE analysis showing tdTomato expression across different cell types in the peripheral blood of tamoxifen-induced *Ms4a3^{CreERT2}-Rosa^{TdT}* mice. Red, high expression; blue, low expression.
 (J) tdTomato labeling in different lymphoid and myeloid lineages of *Ms4a3^{CreERT2}-Rosa^{TdT}* mice induced with tamoxifen (n = 4). Experiment was repeated twice. Error bars, SEM.
 (K) *Ms4a3^{CreERT2}-Rosa^{TdT}* mice were given one injection of tamoxifen (1.75 mg); the tdTomato labeling was monitored for 14 days, n = 3–4 for each time point. Error bars, SEM.
 See also Figure S5.

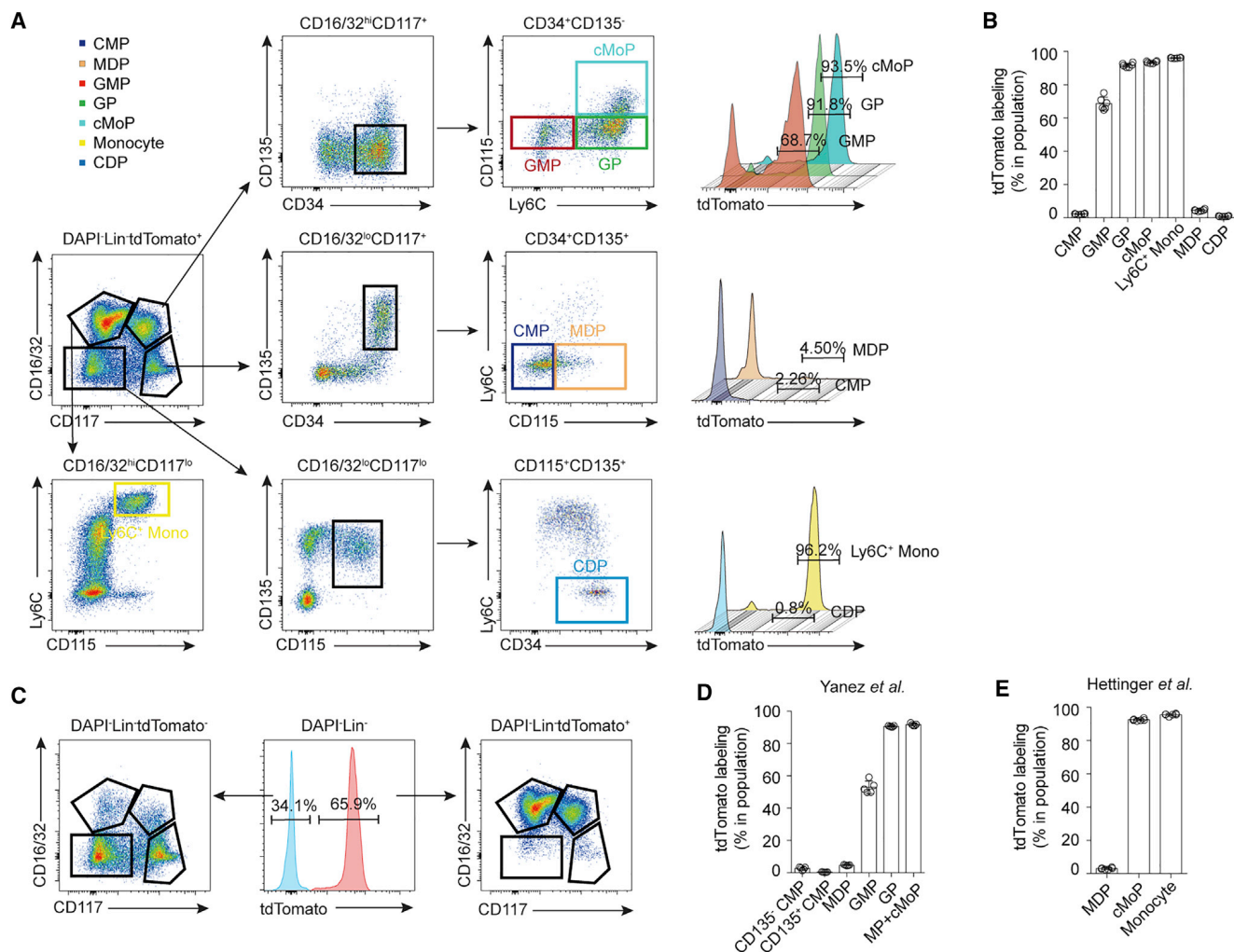


Figure 4. *Ms4a3^{Cre}-Rosa^{TdT}* Labels GMPs in the BM

(A) Gating strategy and tdTomato labeling of BM progenitors in *Ms4a3^{Cre}-Rosa^{TdT}* mice. Histograms show the tdTomato labeling of each population.

(B) tdTomato labeling of indicated progenitor populations in the BM of *Ms4a3^{Cre}-Rosa^{TdT}* mice (n = 6). Error bars, SEM.

(C) tdTomato⁺ and tdTomato⁻ BM cells are separately shown on a CD16/32 versus CD117 plot.

(D) tdTomato labeling of indicated BM progenitors gated with the gating strategy used by Yanez et al. (n = 6). Error bars, SEM.

(E) tdTomato labeling of BM MDPs, cMoPs, and Ly6C⁺ monocytes in the BM, gated with the gating strategy used by Hettinger et al. (n = 6). Error bars, SEM.

See also Figure S6.

and granulocytes were labeled, we analyzed tdTomato labeling in BM progenitor cells in *Ms4a3^{Cre}-Rosa^{TdT}* mice. As predicted, GMPs were the earliest progenitors to be highly labeled (68.7% ± 1.58%), and almost all GMP progenies, such as cMoPs (93.5% ± 0.251%) and GPs (91.8% ± 0.490%) were labeled (Figures 4A and 4B). However, MDPs were lowly labeled (4.5% ± 0.23%) (Figures 4A and 4B). Reverse analysis by first gating on tdTomato⁺ cells showed that almost all tdTomato⁺ cells were CD16/32^{hi}, containing GMPs, cMoPs, GPs, monocytes, and neutrophils (Figures 4C and S6A), while tdTomato⁻ cells were mainly CD16/32^{lo}, containing CMPs, MDPs, and DC precursors (Figures 4C and S6B).

Importantly, MDPs were initially described as Cx3cr1-GFP⁺ CD117⁺CD11b⁻ cells (Fogg et al., 2006), but alternate gating strategies to identify them were proposed, bypassing the

need of the *Cx3cr1^{gfp}* reporter model (Hettinger et al., 2013; Yanez et al., 2017). Thus, to be able to identify MDPs as initially described, we crossed our *Ms4a3^{TdT}* with *Cx3cr1^{gfp}* mice. In the initial gating strategy used by Fogg et al., we found part of the MDPs (Lin⁻Cx3cr1-GFP⁺CD117⁺CD11b⁻) to be tdTomato⁺ (Figure S6C). However, this fraction has a similar phenotype to cMoPs (Lin⁻CD115⁺CD117⁺CD135⁻Ly6C⁺) (Figure S6C) described by Hettinger et al. (2013), suggesting that most of the *Cx3cr1-GFP⁺tdTomato⁺* fraction in the initial Fogg et al. MDP gating are likely corresponding to cMoPs. We also applied the gating strategies from Yanez et al. (2017) (Figures 4D and S6D) and Hettinger et al. (2013) (Figures 4E and S6E), in which the *Cx3cr1-GFP* reporter was not used to identify MDPs. In both gating strategies, the *Ms4a3^{Cre}-Rosa^{TdT}* model labeled cMoPs and monocytes but

did not label MDPs (Figures 4D and 4E). These data support the notion that MDPs do not arise from GMPs but arise from CMPs (Yanez et al., 2017).

MDPs Do Not Arise from GMPs and Do Not Give Rise to cMoPs

Our *Ms4a3^{Cre}-Rosa^{TdT}* model labeled GMPs, cMoPs, and monocytes but did not label CMPs and MDPs, in agreement with the notion that MDPs do not arise from GMPs but arise from CMPs (Yanez et al., 2017). However, not all GMPs were labeled ($68.7\% \pm 1.58\%$), and it could be hypothesized that unlabeled GMPs could give rise to MDPs. To test whether MDPs could still arise from the tdTomato⁻ fraction of GMPs, we sorted tdTomato⁻ GMPs and tdTomato⁻ MDPs and co-cultured them with CD45.1 BM cells in the presence of 50 ng/mL murine M-CSF (CSF-1) for 2 days. Importantly, we did not observe MDP (CD117⁺CD16/32^{lo}CD135⁺CD115⁺) or DC (CD11c⁺MHCII^{+/−}) production by tdTomato⁻ GMPs (Figure 5A) but rather the generation of tdTomato⁺ cMoPs (CD117⁺CD16/32^{hi}CD135⁻CD115⁺Ly6C⁺) (Figure 5A), confirming that MDPs do not arise from GMPs. However, our MDP and cMoP labeling findings (cMoPs were highly labeled in the *Ms4a3^{Cre}-Rosa^{TdT}* model, while MDPs were not) as well as the generation of tdTomato⁺ cMoPs by GMPs but not by MDPs *in vitro* suggest that cMoPs are direct GMP progeny.

However, it is possible that *Ms4a3* expression could be acquired in between MDP and monocyte stages. To test this, we sorted tdTomato⁻ MDPs and tdTomato⁺ and tdTomato⁻ GMPs and cultured *in vitro* for 4 days. We observed that tdTomato⁺ and tdTomato⁻ GMPs gave rise to exactly the same populations in culture, including monocytes, neutrophils, and some macrophages, while MDPs gave rise to DCs, monocytes, and macrophages (Figures 5B and S6F). tdTomato⁻ GMPs and progenies rapidly became tdTomato⁺ ($79.8\% \pm 0.20\%$ at day 1 and $98.6\% \pm 0.25\%$ at day 4), while the tdTomato labeling in tdTomato⁻ MDP culture increased slowly to reach $30.6\% \pm 1.65\%$ at day 4 (Figure 5C). MDP progeny included monocytes and DCs (CD11c⁺MHCII^{+/−}); among them, CD11c⁺ cells were not labeled ($1.00\% \pm 0.14\%$), while monocytes were highly labeled ($75.1\% \pm 2.6\%$) (Figure 5D). These data suggest that *Ms4a3* also labeled MDP-derived monocytes.

To further confirm these findings *in vivo*, we sorted tdTomato⁻ GMPs, tdTomato⁺ GMPs, and tdTomato⁻ MDPs from *Ms4a3^{Cre}-Rosa^{TdT}* mice and adoptively transferred them into CD45.1 recipients. Consistent with the *in vitro* culture observations, tdTomato⁻ GMPs rapidly became tdTomato⁺ and gave rise to monocytes and neutrophils but not to MDPs nor DCs (CD11c⁺) (Figures 5E–5G and S6G). In contrast, MDPs gave rise to CD11c⁺MHCII⁻ (likely to be DC precursors) and monocytes, but not to neutrophils (Figures 5E, 5F, and S6G). Importantly, GMP-derived monocytes were fully labeled (100%). MDP-derived monocytes were also highly labeled ($85.3\% \pm 3.60\%$), while MDP-derived CD11c⁺MHCII⁻ cells were not ($1.51\% \pm 0.82\%$) (Figure 5H). Both tdTomato⁻ and tdTomato⁺ GMPs gave rise to monocytes through an identifiable cMoP (CD117⁺CD16/32^{hi}CD135⁻CD34⁺CD115⁺Ly6C⁺) stage at day 1 but more clearly at day 2 (Figure 5E), while MDPs seem to give rise to monocytes through a different pathway, as we did not identify a cMoP

intermediate in these experiments. MDPs lost CD117 expression from day 1, becoming tdTomato⁻CD117⁻CD16/32^{lo} cells that differentiate into tdTomato⁺CD117⁻CD16/32^{hi}CD115⁺Ly6C⁺ monocytes within 4 days (Figure 5E; data not shown). In summary, the use of *Ms4a3^{Cre}-Rosa^{TdT}* model revealed that MDPs do not arise from GMPs and give rise to monocytes without going through a cMoP stage as commonly accepted.

Monocytes Do Not Contribute Significantly to Tissue DCs with Age

To determine whether tdTomato labeling fluctuates with age, we analyzed peripheral blood cells and splenic DCs from *Ms4a3^{Cre}-Rosa^{TdT}* mice from birth up to 36 weeks. In the peripheral blood, we detected stable and efficient labeling of monocytes and neutrophils (Figures 6A and S7A) and no labeling of lymphocytes (Figure S7A). In the spleen, we found very low, but stable, cDC labeling and no pDC labeling (Figure S7B). Using a gating strategy previously proposed to identify cDCs in murine tissues (Guilliams et al., 2016), we also showed that tissue DCs exhibited very low labeling at 4 weeks (Figure S7C). When investigating whether monocyte-derived cells could accumulate in DC populations with age, we found slightly higher labeling of cDC2 at 12 weeks (Figure S7D). Identifying cDC2s is notoriously less straightforward than cDC1s, as cDC2-specific markers allowing unambiguous identification have not been formally identified. This population may therefore suffer from possible contamination by monocyte-derived cells. Whether such increase reflects a true contribution or contamination of monocytes to the DC pool remains to be investigated. This finding highlights that care must be taken to exclude monocyte-derived cells when identifying cDC2s in non-lymphoid tissues and that our model may help to address this issue in the future.

The Contribution of Monocytes to RTMs Differs under Steady State between Organs and Shows a Tissue-Specific Gender Bias

To investigate the kinetics of RTM replenishment by monocytes in *Ms4a3^{Cre}-Rosa^{TdT}* mice, we analyzed the tdTomato labeling in RTMs in various tissues (brain, epidermis, liver, lung, peritoneal cavity, kidney, spleen, colon, small intestine, and dermis) at different ages (postnatal 0, 2 weeks, 4 weeks, 8 weeks, 20 weeks, 36 weeks). Of note, the labeling of blood monocytes was very efficient from birth (Figure 6A), whereas the labeling of tissue RTMs was negligible in newborn mice (Figures 6B–6E). This finding suggests that our fate-mapping model does not label embryonic macrophages or their precursors during development. In accordance with published reports, we found no postnatal changes in tdTomato labeling in brain microglia, epidermal LCs, or liver KCs during steady-state development (Figure 6B); conversely, tdTomato labeling in macrophages slowly increased with age in the lung, spleen, peritoneal cavity, and kidney (Figure 6C). As expected (Bain et al., 2016), we observed a rapid increase in tdTomato labeling in macrophages in the colon and small intestine over the first 8 weeks after birth, with a faster rate in the colon than in the small intestine (Figure 6D). Also in accordance with a previous report (Tamoutounour et al., 2013), dermal MHCII⁺ macrophages were replaced faster than MHCII⁻ macrophages (Figure 6E). We confirmed

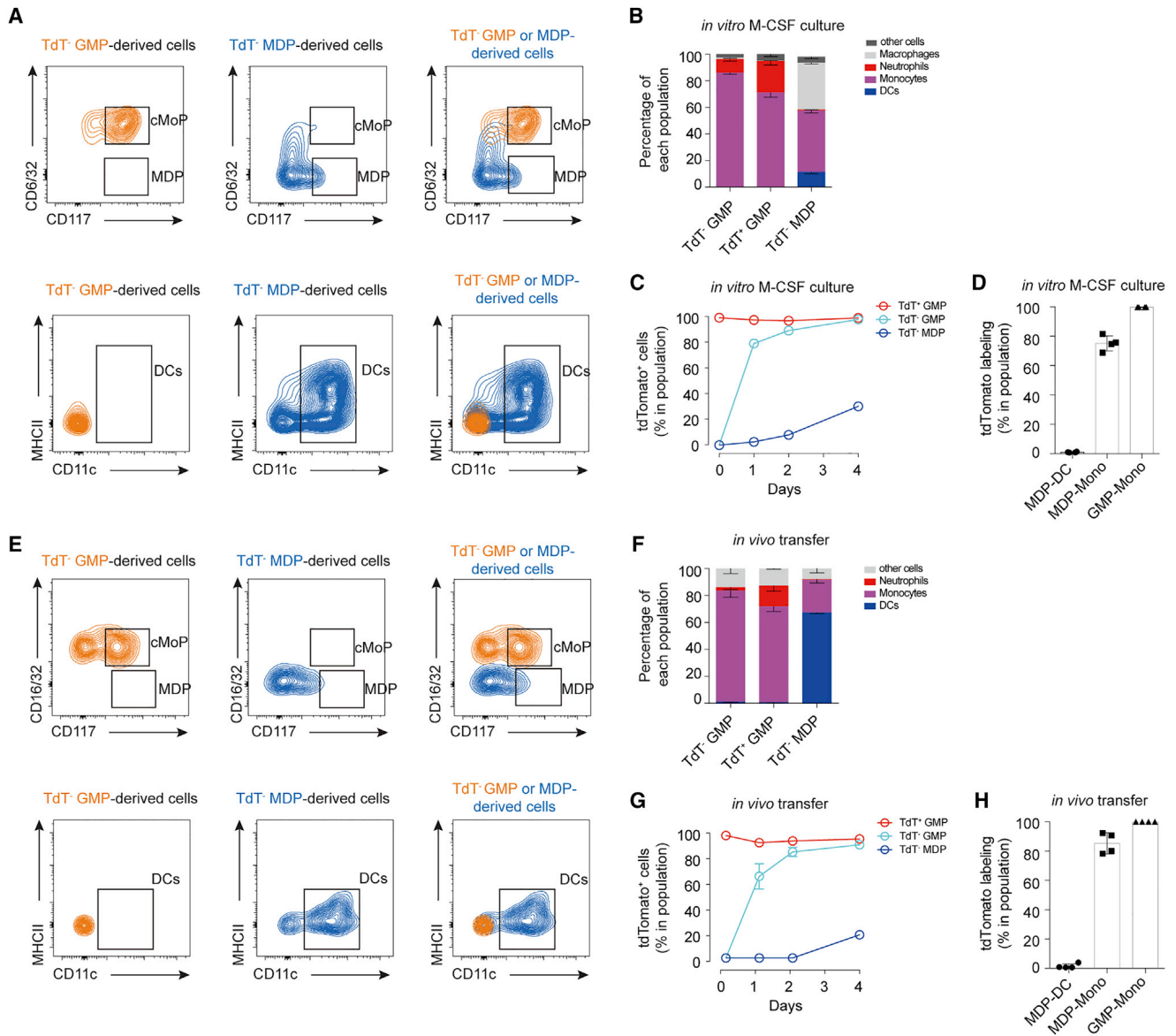


Figure 5. GMPs Do Not Give Rise to MDPs *In Vitro* and *In Vivo*

(A) tdTomato⁻ GMPs (orange) and tdTomato⁻ MDPs (blue) were cultured *in vitro* for 2 days, and production of MDPs, DCs, cMoPs, and monocytes was analyzed by flow cytometry. Experiment was repeated more than three times.

(B) Production of DCs, monocytes, neutrophils, and macrophages by indicated progenitors were analyzed by flow cytometry at day 4 of *in vitro* culture (n = 4). Experiment was repeated more than three times. Error bars, SEM.

(C) tdTomato labeling kinetics of indicated progenitor populations cultured *in vitro* as described in (A). Experiment was repeated twice with four replicates in each experiment. Error bars, SEM.

(D) tdTomato labeling in tdTomato⁻ MDP-derived DCs, tdTomato⁻ MDP-derived monocytes, and tdTomato⁻ GMP-derived monocytes at day 4 of culture. Error bars, SEM.

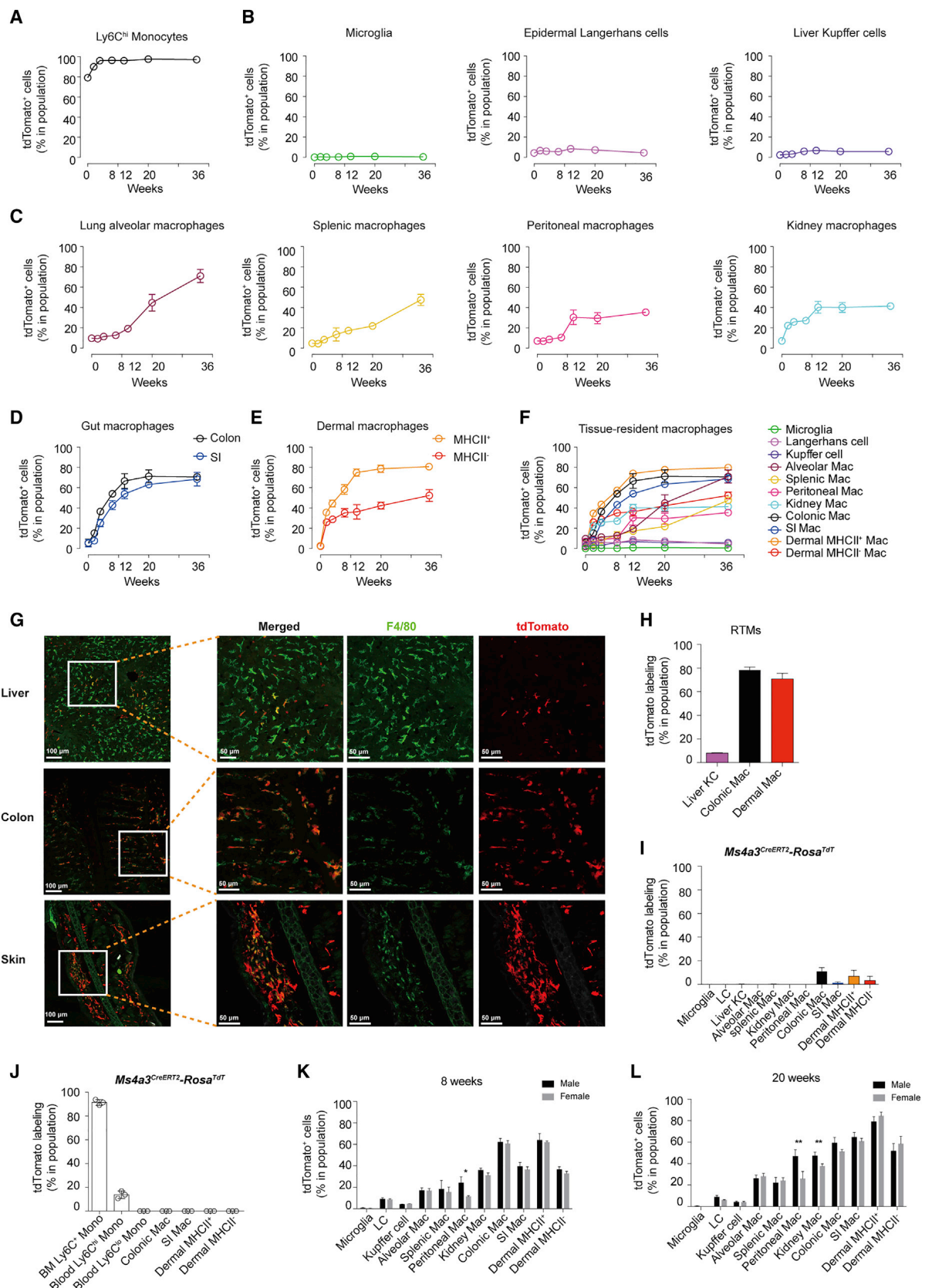
(E) 10,000–20,000 tdTomato⁻ GMPs (orange) and tdTomato⁻ MDPs (blue) were adoptively transferred i.v. into non-irradiated CD45.1 recipient mice. The production of MDPs, DCs, cMoPs, and monocytes in the BM were analyzed by flow cytometry at day 2.

(F) Production of DCs, monocytes, and neutrophils by indicated progenitors was analyzed by flow cytometry at day 4 after adoptive transfer (n = 4). Error bars, SEM.

(G) tdTomato labeling kinetics of indicated progenitor populations *in vivo* as described in (E). Experiment was repeated twice. Error bars, SEM.

(H) tdTomato labeling in tdTomato⁻ MDP-derived DCs, tdTomato⁻ MDP-derived monocytes, and GMP-derived monocytes at day 4 of *in vivo* adoptive transfer. Experiment was repeated three times. Error bars, SEM.

See also Figure S6.



(legend on next page)

our flow-cytometry-based observations (Figure 6F) by immunofluorescence analysis of the corresponding tissues (Figure 6G). Most liver F4/80⁺ cells (92% ± 0.15%) likely to be KCs were tdTomato⁻, in agreement with their embryonic origin, while most of the gut (78% ± 1.24%) and dermal (70% ± 2.75%) F4/80⁺ macrophages were tdTomato⁺, underlining their derivation from tdTomato⁺ monocytes (Figures 6G and 6H). In a parallel comparison to our models, we analyzed the labeling of RTMs in *Cx3cr1^{Cre}-Rosa^{TdT}* and *Cx3cr1^{CreERT2}-Rosa^{TdT}*. In the *Cx3cr1^{Cre}-Rosa^{TdT}*, all RTMs were labeled, including the RTMs negative for Cx3cr1 expression (LCs, KCs, AMs, splenic macrophages, and some dermal macrophages), reflecting the contribution of Cx3cr1⁺ embryonic precursors (Figure S7E). In *Cx3cr1^{CreERT2}-Rosa^{TdT}* mice, as predicted, microglia, gut macrophages, and kidney macrophages were fully labeled; other RTMs were either not labeled or labeled to a lesser extent based on their selective expression of Cx3cr1 (Figure S7F).

To formally exclude the intrinsic expression of Ms4a3 in RTMs that could contribute to their labeling in the constitutive *Ms4a3^{Cre}-Rosa^{TdT}* fate-mapping model, we took advantage of the *Ms4a3^{CreERT2}-Rosa^{TdT}*-inducible model. Mice were treated with four injections of tamoxifen i.p. or gavage (for peritoneal macrophage analysis), and RTM labeling was analyzed at day 7. While blood monocytes were fully labeled (Figure 3K), only gut and dermal macrophages exhibited minor tdTomato labeling (Figure 6I). Such low labeling, rather than expression of Ms4a3 by macrophages, likely reflects the recent recruitment and differentiation from monocytes within the experimental time window of 7 days. Thus, we gave one injection of tamoxifen to *Ms4a3^{CreERT2}-Rosa^{TdT}* mice and analyzed the labeling 24 h after. BM Ly6C^{hi} monocytes were fully labeled (91.4% ± 1.36%), while blood Ly6C^{hi} monocytes were lowly labeled (13.8% ± 1.82%) (Figure 6J). Importantly, no tdTomato labeling was detected in gut or dermal macrophages (Figure 6J). Combined with the *Ms4a3^{TdT}* reporter mouse data where no reporter signal was detected (Figures S4A–S4I), we conclude that RTMs do not express Ms4a3 and that the tdTomato⁺ labeling in RTMs accurately reflects blood monocyte contribution.

To investigate the gender bias in RTM renewal, we compared the labeling of various RTM populations in males and females at

8 weeks and 20 weeks (Figures 6K and 6L). At 8 weeks, among the RTM populations analyzed, only peritoneal macrophages showed a significant difference between males and females (Figure 6K). At 20 weeks, however, we observed that peritoneal macrophages and kidney macrophages significantly differed between males and females (Figure 6L), consistent with a previous report (Bain et al., 2016). In summary, we confirmed using our fate-mapping model that the contribution of monocytes to RTMs differed between organs during steady-state conditions but also by gender in peritoneal and kidney macrophages.

Monocyte Contribution to RTMs during Inflammation Is Model Dependent

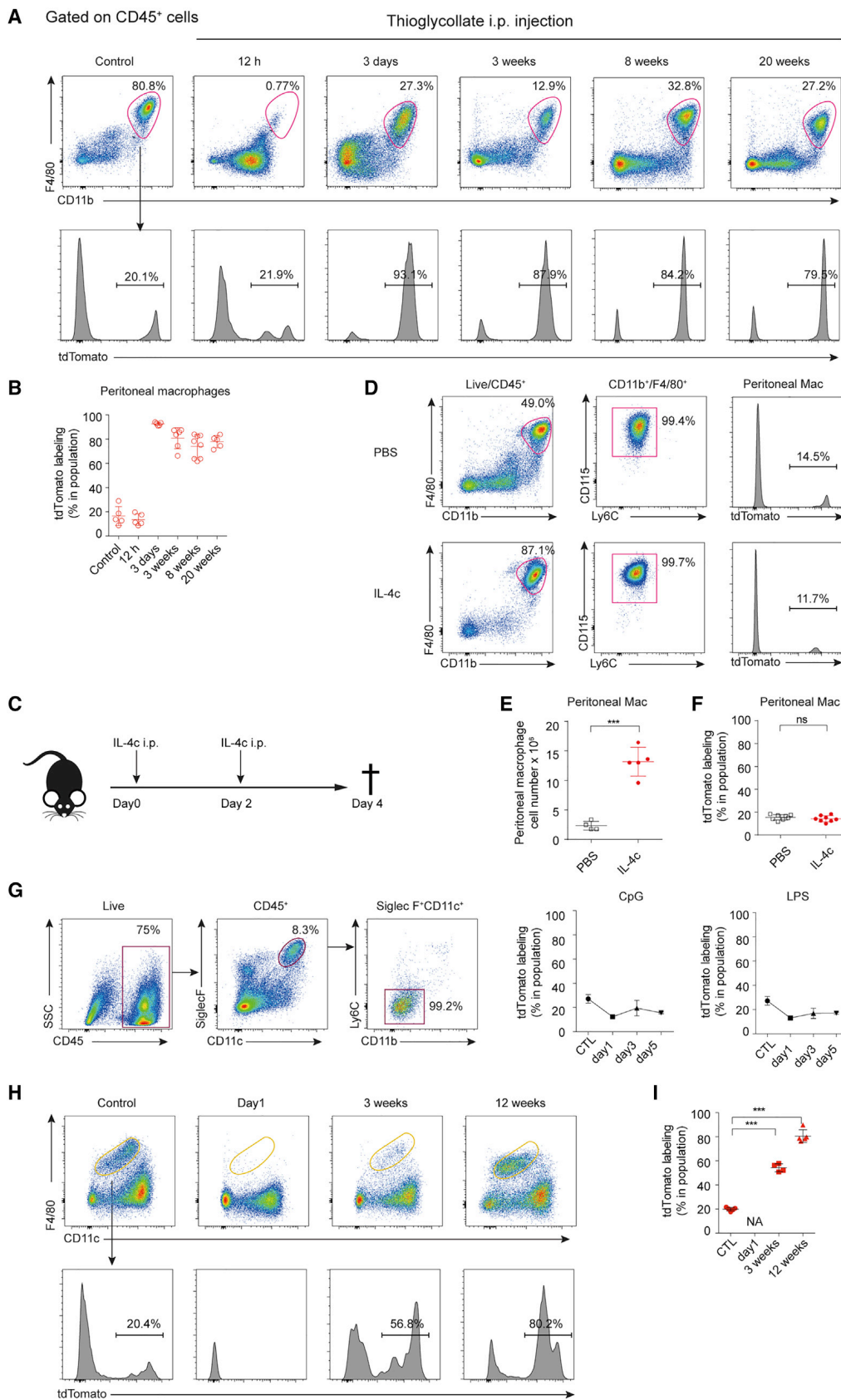
Inflammatory stimuli often induce monocyte recruitment; these monocytes might potentially contribute to RTMs upon the resolution of inflammation. To investigate the contribution of circulating monocytes to RTMs during inflammation, we established various experimental scenarios of inflammation, including (1) thioglycollate-induced peritonitis, (2) IL-4; anti-IL-4 complex (IL-4c) stimulation, (3) lipopolysaccharide (LPS)-induced peritonitis, (4) LPS and cytosine guanine dinucleotide (CpG) lung stimulation, and (5) clodronate-loaded liposome-mediated macrophage depletion.

In the thioglycollate-induced peritonitis model, we observed a marked decrease in the number of peritoneal macrophages at 12 h, which was concomitant with an increase in the relative number of DAPI⁺ peritoneal macrophages, suggestive of induced peritoneal macrophage cell death (Figures 7A, S7G, and S7H). From day 3, tdTomato labeling of peritoneal macrophages was significantly higher (74.1%–92.6%) compared to the steady-state control (16.6% ± 3.478%), suggesting replacement by monocytes (Figure 7B). To formally exclude the intrinsic expression of Ms4a3 in RTMs during this inflammatory challenge, we sorted peritoneal macrophages at different time points after thioglycollate administration and performed RNA-seq. We did not detect any significant level of Ms4a3 expression in peritoneal macrophages at any time point tested (Figure S7I). We also performed a similar challenge in the *Ms4a3^{CreERT2}-Rosa^{TdT}* mice after tamoxifen gavage for 4 days and 3 days chase. At day 7, just before induction of thioglycollate-induced peritonitis,

Figure 6. The Contribution of Monocytes to RTMs Differs among Organs and Shows a Tissue-Specific Gender Bias

- (A) Labeling kinetics of tdTomato in blood Ly6C^{hi} monocytes in *Ms4a3^{Cre}-Rosa^{TdT}* mice at different ages, as indicated. Error bars, SEM.
- (B) Labeling kinetics of tdTomato in microglia (CD45^{int}CD11b⁺F4/80⁺Ly6C⁻), epidermal LCs (CD45⁺Thy1⁻CD11b⁺F4/80⁺EpCAM⁺), and liver KCs (CD45⁺CD11b⁺F4/80⁺Tim-4⁺) in *Ms4a3^{Cre}-Rosa^{TdT}* mice at different ages, as indicated. Error bars, SEM.
- (C) Labeling kinetics of tdTomato in lung AMs (CD45⁺SiglecF⁺CD11c⁺CD11b^{lo}Ly6C⁻), splenic macrophages (CD45⁺Lin⁻F4/80⁺), peritoneal macrophages (CD45⁺CD11b^{hi}F4/80^{hi}), and kidney macrophages (CD45⁺CD11b⁺F4/80⁺MHCII⁺) in *Ms4a3^{Cre}-Rosa^{TdT}* mice at different ages, as indicated. Error bars, SEM.
- (D) Labeling kinetics of tdTomato in macrophages (CD45⁺SiglecF⁻Ly6G⁻CD11b⁺CD64⁺CD11c⁻Ly6C⁻MHCII⁺) in the colon (black) and small intestine (blue) in *Ms4a3^{Cre}-Rosa^{TdT}* mice at different ages, as indicated. Error bars, SEM.
- (E) Labeling kinetics of tdTomato in dermal MHCII⁺ macrophages (CD45⁺CD11b⁺F4/80⁺CD64⁺MHCII⁺) and MHCII⁻ macrophages (CD45⁺CD11b⁺F4/80⁺CD64⁺MHCII⁻) in *Ms4a3^{Cre}-Rosa^{TdT}* mice at different ages, as indicated. Error bars, SEM.
- (F) Summary of the labeling kinetics of tdTomato in RTMs of *Ms4a3^{Cre}-Rosa^{TdT}* mice. n = 3–4 female mice analyzed per time point. Error bars, SEM.
- (G) Confocal imaging showing tdTomato (red) labeling in F4/80⁺ macrophages (green) in the liver, colon, and skin of 12-week-old female *Ms4a3^{Cre}-Rosa^{TdT}* mice.
- (H) Relative numbers of tdTomato⁺ cells in F4/80⁺ macrophages in liver, colon, and skin in confocal image from (G). Error bars, SEM.
- (I) tdTomato labeling in RTMs of *Ms4a3^{CreERT2}-Rosa^{TdT}* mice induced with tamoxifen (n = 4). Error bars, SEM.
- (J) tdTomato labeling in RTMs of *Ms4a3^{CreERT2}-Rosa^{TdT}* mice induced with 1 injection of tamoxifen and analyzed at 24 h (n = 3). Error bars, SEM.
- (K) tdTomato labeling of RTM populations from 8-week-old male (black) and female (gray) mice. n = 3 mice per sex. Error bars, SEM.
- (L) tdTomato labeling of RTM populations from 20-week-old male (black) and female (gray) mice. n = 3 mice per sex. Statistical significance is indicated by *p < 0.05, **p < 0.01. Error bars, SEM.

See also Figure S7.



(legend on next page)

we analyzed the peripheral blood and peritoneal macrophages. Blood Ly6C^{hi} monocytes were highly labeled (93.7% ± 1.14%), while peritoneal macrophages were not (0.03% ± 0.01%) (Figure S7J). We then analyzed the same populations 72 h after. Blood Ly6C^{hi} monocytes labeling decreased (51.2% ± 5.75%), while peritoneal macrophages were highly labeled (87.3% ± 1.18%), suggesting that they arise from monocytes (Figure S7J). Altogether, we conclude that peritoneal macrophages do not intrinsically express Ms4a3 and that tdTomato labeling after thioglycollate-induced peritonitis can be attributed to recruited monocytes.

Next, we used IL-4c to induce local macrophage proliferation that is known to occur without a circulating monocyte contribution (Jenkins et al., 2011) (Figures 7C and S7K). As expected, we observed a 4-fold increase in the number of peritoneal macrophages (Figures 7D and 7E), which was not associated with any changes in tdTomato labeling (Figure 7F). This confirmed the numbers of peritoneal macrophages increased through local proliferation of all macrophages irrespective of origin, rather than the recruitment of blood monocytes.

Finally, we induced peritonitis in *Ms4a3^{Cre}-Rosa^{TdT}* mice by LPS i.p. injection. We observed no changes in tdTomato labeling in peritoneal macrophages at any time point, indicating no monocyte contribution to peritoneal macrophages (Figure S7L). It is important to note that in this condition, we did not observe any peritoneal macrophage cell death (Figure S7M). We made similar observations in other organs under inflammation. In LPS- and CpG-induced lung inflammation, we observed no differences in tdTomato labeling of AMs between treated mice and controls despite observing significant monocyte recruitment (Figures 7G and S7N). Again, no significant AM cell death was observed (Figure S7O). In contrast, in the clodronate-induced RTM depletion model, almost all macrophages in the spleen were depleted at day 1 (Figure 7H). By 3 weeks post-depletion, the repopulated macrophages were tdTomato⁺ (control versus clodronate, 19.9% ± 0.56% versus 54.3% ± 1.70% and 80.6% ± 1.38%) (Figures 7I, S7P, and S7Q).

Taken together, our *Ms4a3^{Cre}-Rosa^{TdT}* and *Ms4a3^{CreERT2}-Rosa^{TdT}* fate-mapping models show the contribution of monocytes to RTMs under different inflammatory settings. Our data suggest that monocytes can fill the empty niche left by depleted macrophages and develop into monocyte-derived macrophages.

DISCUSSION

The classical model of hematopoiesis proposes that MDPs arise from GMPs and give rise to monocytes through a cMoP stage (Ginhoux and Jung, 2014; Guillems et al., 2018; Terry and Miller, 2014). In a recent study, Yanez et al. showed that MDPs arise directly from CMPs independently of GMPs and that GMPs and MDPs give rise to monocytes via MPs and cMoPs, respectively (Yanez et al., 2017), although no phenotypic difference between MPs and cMoPs was reported. Our *Ms4a3^{Cre}-Rosa^{TdT}* model labeled GMPs, cMoPs, granulocytes, and monocytes but not MDPs or DCs, providing strong evidence that MDPs do not arise from GMPs as proposed by Yanez et al. Here, we found that MDPs do not give rise to cMoPs and give rise to monocytes and DCs *in vitro* and *in vivo* through a yet-undescribed tdTomato⁻CD117⁻CD16/32^{lo} stage. The nature of such population and its relationship to cMoPs and CDPs remains to be investigated. These results show that monocytes are generated through two distinct cellular pathways defined by complementary oligopotent progenitor populations and raise the question of the nature of GMP- versus MDP-derived monocytes and their physiological relevance in steady state and in inflammation. Furthermore, the existence of the MDP population as an independent and distinct stage of myelopoiesis could be challenged as already discussed by Sathe et al. (2014). Nevertheless, since both GMPs and MDPs give rise to tdTomato⁺ monocytes, it is not yet possible in our *Ms4a3^{Cre}-Rosa^{TdT}* model to discriminate between these two ontogenic pathways. Hence, our Ms4a3 fate mapper traces monocytes without discriminating their origins. Future studies including fate-mapping models of GMPs or MDPs will help to clarify these questions and help to identify the intermediate stages between MDPs and their monocyte progeny.

Using the *Ms4a3^{Cre}-Rosa^{TdT}* model, we systemically assessed the contribution of monocytes to RTMs under steady-state conditions. Our data are concordant with previously published reports, showing that some RTMs have no monocyte contribution (microglia, KCs, and LCs) and that others exhibit a tissue-specific monocyte contribution, as previously proposed (Ginhoux and Guillems, 2016). We also observed fast (gut and dermis) versus slow (kidney, spleen, and peritoneum) RTM replacement. We also confirmed that in the dermis, MHCII⁺ macrophages are replaced at a faster rate than MHCII⁻ macrophages

Figure 7. Monocyte Contribution to RTMs during Inflammation Is Model Dependent

- (A) Flow cytometric analysis of peritoneal lavage from *Ms4a3^{Cre}-Rosa^{TdT}* mice at the indicated time points after i.p. injection of thioglycollate.
- (B) tdTomato labeling in peritoneal macrophages at the indicated time points after i.p. thioglycollate injection. The data are representative of two independent experiments with 5–8 female mice per group. Error bars, SEM.
- (C) Experimental protocol. Mice were injected with IL-4c on days 0 and 2 and analyzed on day 4.
- (D) Flow cytometric analysis of peritoneal lavage from *Ms4a3^{Cre}-Rosa^{TdT}* mice injected with IL-4c or PBS control.
- (E) The absolute numbers of peritoneal macrophages in the peritoneal lavage isolated from female mice injected with IL-4c or PBS, n = 4–5 female mice per group. Error bars, SEM.
- (F) tdTomato labeling in peritoneal macrophages from mice injected with IL-4c or PBS, n = 4–9 female mice per group. Error bars, SEM.
- (G) Flow cytometric analysis of lung AMs in *Ms4a3^{Cre}-Rosa^{TdT}* mice treated with 10 μg LPS or 50 μg CpG i.n.; tdTomato labeling of AMs was analyzed at the indicated time points, n = 3–4 mice for each time point. Error bars, SEM.
- (H) Flow cytometric analysis of splenic macrophages from *Ms4a3^{Cre}-Rosa^{TdT}* mice at the indicated time points after i.v. injection of 200 μL clodronate liposome, n = 4–5 for each group.
- (I) tdTomato labeling in splenic macrophages from *Ms4a3^{Cre}-Rosa^{TdT}* mice after macrophage depletion by clodronate liposome i.v. injection, n = 4–5 for each group. Statistical significance is indicated by ***p < 0.001; ns, not significant. Error bars, SEM.
- See also Figure S7.

(Tamoutounour et al., 2013). These results highlight that within tissues, subpopulations of macrophages coexist with a unique homeostatic regime. The mechanisms underlying this heterogeneity could be attributed to differences in the environmental niches within the tissue or at the sub-tissular level. In agreement with this hypothesis, we recently showed that two independent monocyte-derived RTM populations coexist across tissues with distinct functional profiles in unique sub-tissular niches: a Lyve1^{lo}MHCII^{hi}CX3CR1^{hi} population that is mostly found surrounding the nerves and a Lyve1^{hi}MHCII^{lo}CX3CR1^{lo} population that is often closely associated with blood vessels across tissues (Chakarov et al., 2019).

None of the RTM populations that showed a significant contribution from monocytes with time—in particular dermal MHCII⁺ and gut (of which most are MHCII⁺) macrophages—exhibited total replacement by monocytes. The level of replacement reached its asymptote, for example ~12 weeks for dermal MHCII⁺ and gut macrophages, and no further increase was observed thereafter. These results suggest that at its asymptotic phase, the tissue likely reaches an equilibrium of monocyte recruitment, proliferation, and survival or death between adult-derived RTMs and proliferation and survival or death of embryonic-derived RTMs. Future studies are warranted to formally establish the exact contribution of monocyte recruitment, proliferation, and survival or death at these later time points in each RTM population. Furthermore, it should be ascertained whether such equilibrium is not the result of heterogeneous populations in origin residing in different sub-tissular localizations, for each tissue macrophage population or subpopulation studied. Nevertheless, for more defined populations of macrophages with a known niche, our observations suggest that tissues reach equilibrium in terms of macrophage homeostasis after 12 weeks. This equilibrium might simply reflect a sign of tissue maturity in terms of niche availability—a speculation that would be in agreement with the notion that macrophage homeostasis is controlled by niche access or availability (Guilliams and Scott, 2017). The implications of these ideas are important: they suggest that if tissue maturity in terms of macrophage content is not reached before 20 weeks, the most commonly chosen 6–8-week experimental time point used as a surrogate of adulthood may be premature.

Using our *Ms4a3^{Cre}-Rosa^{TdT}* mouse model, we also found that the contribution of monocytes to macrophages differs according to sex and the challenge used to induce inflammation. These results highlight that the mechanisms behind different RTM renewal patterns are not fully understood and are likely controlled by the microenvironment, age, sex, and/or other factors such as the microbiome or diet; these mechanisms can now be readily tested by the scientific community using our models. In addition, we found that under inflammatory conditions that deplete RTMs (such as thioglycollate-induced peritonitis), monocytes infiltrate the tissue and replenish the macrophage population, while under inflammatory conditions that do not deplete RTMs (such as LPS-induced and CpG-induced lung inflammation and LPS-induced peritonitis), we did not observe a contribution of monocytes to RTMs. These observations again support the hypothesis that monocyte contribution to RTMs is subject to niche access and availability (Guilliams and Scott, 2017).

In conclusion, *Ms4a3^{TdT}* reporter, and *Ms4a3^{Cre}*, and *Ms4a3^{CreERT2}* fate-mapping models permit the precise and faithful identification of monocytes and monocyte-derived cells in any condition and disentangle monocyte-derived macrophages from embryonic RTMs. These models will be critical to improve our understanding of the function of embryonic RTMs and BM-derived macrophages in homeostasis and inflammation and other models of disease including infection, cancer, and metabolic diseases.

LIMITATIONS

Although *Ms4a3*-based models clearly fate map monocytes and granulocytes, they could not distinguish monocytes with different origins (GMPs versus MDPs). Furthermore, although we did not observe any intrinsic labeling in RTMs in steady-state or inflammation settings tested here, we cannot formally exclude that few rare RTMs could start to express *Ms4a3* in certain conditions not tested here, raising the need for complementary models that fate map only embryonic macrophages but not monocyte-derived macrophages.

STAR★METHODS

Detailed methods are provided in the online version of this paper and include the following:

- KEY RESOURCES TABLE
- LEAD CONTACT AND MATERIALS AVAILABILITY
- EXPERIMENTAL MODEL AND SUBJECT DETAILS
 - Animals
- METHOD DETAILS
 - Single cell RNA-sequencing (scRNA-seq)
 - scRNA-seq data analysis
 - Quantitative Real-Time PCR (qRT-PCR)
 - Tissue preparation for flow cytometry
 - Flow Cytometry
 - Cell Sorting
 - *In vitro* culture
 - *In vivo* transfer
 - Confocal microscopy
 - Tamoxifen induction
 - Inflammatory models
 - Bulk RNA Sequencing
 - Macrophage depletion with clodronate liposome
- QUANTIFICATION AND STATISTICAL ANALYSIS
 - Statistical analysis
- DATA AND CODE AVAILABILITY

ACKNOWLEDGMENTS

F.G. is an EMBO YIP awardee and is supported by Singapore Immunology Network (SIgN) core funding as well as a Singapore National Research Foundation Senior Investigatorship (NRF) NRF2016NRF-NRFI001-02. Some experiments were done with the help of the SIgN Immunomonitoring platform (bioinformatics and immunogenomics platforms supported by a BMRC IAF 311006 grant and BMRC transition funds #H16/99/b0/011). This work was supported by the National Natural Science Foundation of China (NSFC) (31470845, 81430033, and 31670896 to B.S.) and Shanghai Science and

Technology Commission (SSTC) (13JC1404700 to B.S.). Zhiduo L. was supported by NSFC (31870871) and SSTC (17PJ1408300 and 17ZR1425000). The authors would like to thank the flow core, sequencing core, and imaging core of Shanghai Institute of Immunology for their support. The authors would also like to thank Insight Editing London for editing the manuscript prior to submission.

AUTHOR CONTRIBUTIONS

Zhaoyuan L., Y.G., S.C., C.B., I.K., X.C., A. Shin, W.H., R.J.D., and A. Schlitzer conducted the experiments; Zhaoyuan L., S.C., C.B., J.C., C.-A.D., B.S., and F.G. analyzed the data; Zhaoyuan L. and F.G. wrote the paper; H.W., Zhiduo L., and L.G.N. provided intellectual input; B.S. and F.G. supervised the project; F.G. conceptualized the study.

DECLARATION OF INTERESTS

The authors declare no competing interests.

Received: January 22, 2019

Revised: June 13, 2019

Accepted: August 6, 2019

Published: September 5, 2019

REFERENCES

- Auffray, C., Fogg, D.K., Narni-Mancinelli, E., Senechal, B., Trouillet, C., Sæderup, N., Leemput, J., Bigot, K., Campisi, L., Abitbol, M., et al. (2009). CX3CR1+ CD115+ CD135+ common macrophage/DC precursors and the role of CX3CR1 in their response to inflammation. *J. Exp. Med.* *206*, 595–606.
- Bain, C.C., Bravo-Blas, A., Scott, C.L., Perdiguero, E.G., Geissmann, F., Henri, S., Malissen, B., Osborne, L.C., Artis, D., and Mowat, A.M. (2014). Constant replenishment from circulating monocytes maintains the macrophage pool in the intestine of adult mice. *Nat. Immunol.* *15*, 929–937.
- Bain, C.C., Hawley, C.A., Garner, H., Scott, C.L., Schridde, A., Steers, N.J., Mack, M., Joshi, A., Guilliams, M., Mowat, A.M., et al. (2016). Long-lived self-renewing bone marrow-derived macrophages displace embryo-derived cells to inhabit adult serous cavities. *Nature Commun.* *7*, ncomms11852.
- Blériot, C., Dupuis, T., Jouvion, G., Eberl, G., Disson, O., and Lecuit, M. (2015). Liver-resident macrophage necroptosis orchestrates type 1 microbicidal inflammation and type-2-mediated tissue repair during bacterial infection. *Immunity* *42*, 145–158.
- Chakarov, S., Lim, H.Y., Tan, L., Lim, S.Y., See, P., Lum, J., Zhang, X.M., Foo, S., Nakamizo, S., Duan, K., et al. (2019). Two distinct interstitial macrophage populations coexist across tissues in specific subtissular niches. *Science* *363*, eaau0964.
- Clausen, B.E., Burkhardt, C., Reith, W., Renkawitz, R., and Förster, I. (1999). Conditional gene targeting in macrophages and granulocytes using LysMcre mice. *Transgenic Res.* *8*, 265–277.
- Donato, J.L., Ko, J., Kutok, J.L., Cheng, T., Shirakawa, T., Mao, X.Q., Beach, D., Scadden, D.T., Sayegh, M.H., and Adra, C.N. (2002). Human HTm4 is a hematopoietic cell cycle regulator. *J. Clin. Invest.* *109*, 51–58.
- Dress, R.J., Dutertre, C.A., Giladi, A., Schlitzer, A., Low, I., Shadan, N.B., Tay, A., Lum, J., Kairi, M.F.B.M., Hwang, Y.Y., et al. (2019). Plasmacytoid dendritic cells develop from Ly6D⁺ lymphoid progenitors distinct from the myeloid lineage. *Nat. Immunol.* *20*, 852–864.
- Ensan, S., Li, A., Besla, R., Degousee, N., Cosme, J., Roufaiel, M., Shikatani, E.A., El-Maklizi, M., Williams, J.W., Robins, L., et al. (2016). Self-renewing resident arterial macrophages arise from embryonic CX3CR1 precursors and circulating monocytes immediately after birth. *Nat. Immunol.* *17*, 159–168.
- Feil, R., Wagner, J., Metzger, D., and Chambon, P. (1997). Regulation of Cre recombinase activity by mutated estrogen receptor ligand-binding domains. *Biochem. Biophys. Res. Commun.* *237*, 752–757.
- Fogg, D.K., Sibon, C., Miled, C., Jung, S., Aucouturier, P., Littman, D.R., Cuman, A., and Geissmann, F. (2006). A clonogenic bone marrow progenitor specific for macrophages and dendritic cells. *Science* *311*, 83–87.
- Giladi, A., Paul, F., Herzog, Y., Lubling, Y., Weiner, A., Yofe, I., Jaitin, D., Cabezas-Wallscheid, N., Dress, R., Ginhoux, F., et al. (2018). Single-cell characterization of haematopoietic progenitors and their trajectories in homeostasis and perturbed haematopoiesis. *Nat. Cell Biol.* *20*, 836–846.
- Ginhoux, F., and Guilliams, M. (2016). Tissue-Resident Macrophage Ontogeny and Homeostasis. *Immunity* *44*, 439–449.
- Ginhoux, F., and Jung, S. (2014). Monocytes and macrophages: developmental pathways and tissue homeostasis. *Nat. Rev. Immunol.* *14*, 392–404.
- Ginhoux, F., Greter, M., Leboeuf, M., Nandi, S., See, P., Gokhan, S., Mehler, M.F., Conway, S.J., Ng, L.G., Stanley, E.R., et al. (2010). Fate mapping analysis reveals that adult microglia derive from primitive macrophages. *Science* *330*, 841–845.
- Guilliams, M., and Scott, C.L. (2017). Does niche competition determine the origin of tissue-resident macrophages? *Nat. Rev. Immunol.* *17*, 451–460.
- Guilliams, M., De Kleer, I., Henri, S., Post, S., Vanhoutte, L., De Prijck, S., Deswarte, K., Malissen, B., Hammad, H., and Lambrecht, B.N. (2013). Alveolar macrophages develop from fetal monocytes that differentiate into long-lived cells in the first week of life via GM-CSF. *J. Exp. Med.* *210*, 1977–1992.
- Guilliams, M., Dutertre, C.A., Scott, C.L., McGovern, N., Sichien, D., Chakarov, S., van Gassen, S., Chen, J., Poidinger, M., De Prijck, S., et al. (2016). Unsupervised High-Dimensional Analysis Aligns Dendritic Cells across Tissues and Species. *Immunity* *45*, 669–684.
- Guilliams, M., Mildner, A., and Yona, S. (2018). Developmental and Functional Heterogeneity of Monocytes. *Immunity* *49*, 595–613.
- Hashimoto, D., Chow, A., Noizat, C., Teo, P., Beasley, M.B., Leboeuf, M., Becker, C.D., See, P., Price, J., Lucas, D., et al. (2013). Tissue-resident macrophages self-maintain locally throughout adult life with minimal contribution from circulating monocytes. *Immunity* *38*, 792–804.
- Heng, T.S., and Painter, M.W.; Immunological Genome Project Consortium (2008). The Immunological Genome Project: networks of gene expression in immune cells. *Nat. Immunol.* *9*, 1091–1094.
- Hettinger, J., Richards, D.M., Hansson, J., Barra, M.M., Joschko, A.C., Krijgsveld, J., and Feuerer, M. (2013). Origin of monocytes and macrophages in a committed progenitor. *Nat. Immunol.* *14*, 821–830.
- Hoefel, G., and Ginhoux, F. (2015). Ontogeny of Tissue-Resident Macrophages. *Front. Immunol.* *6*, 486.
- Hoefel, G., Wang, Y., Greter, M., See, P., Teo, P., Malleret, B., Leboeuf, M., Low, D., Oller, G., Almeida, F., et al. (2012). Adult Langerhans cells derive predominantly from embryonic fetal liver monocytes with a minor contribution of yolk sac-derived macrophages. *J. Exp. Med.* *209*, 1167–1181.
- Hulett, M.D., Pagler, E., and Hornby, J.R. (2001). Cloning and characterization of a mouse homologue of the human haematopoietic cell-specific four-transmembrane gene HTm4. *Immunol. Cell Biol.* *79*, 345–349.
- Ingersoll, M.A., Spanbroek, R., Lottaz, C., Gautier, E.L., Frankenberger, M., Hoffmann, R., Lang, R., Haniffa, M., Collin, M., Tacke, F., et al. (2010). Comparison of gene expression profiles between human and mouse monocyte subsets. *Blood* *115*, e10–e19.
- Jenkins, S.J., Ruckerl, D., Cook, P.C., Jones, L.H., Finkelman, F.D., van Rooijen, N., MacDonald, A.S., and Allen, J.E. (2011). Local macrophage proliferation, rather than recruitment from the blood, is a signature of TH2 inflammation. *Science* *332*, 1284–1288.
- Jung, S., Aliberti, J., Graemmel, P., Sunshine, M.J., Kreutzberg, G.W., Sher, A., and Littman, D.R. (2000). Analysis of fractalkine receptor CX3CR1 function by targeted deletion and green fluorescent protein reporter gene insertion. *Mol. Cell. Biol.* *20*, 4106–4114.
- Lamb, J., Crawford, E.D., Peck, D., Modell, J.W., Blat, I.C., Wrobel, M.J., Lerner, J., Brunet, J.P., Subramanian, A., Ross, K.N., et al. (2006). The Connectivity Map: using gene-expression signatures to connect small molecules, genes, and disease. *Science* *313*, 1929–1935.

- Madisen, L., Zwingman, T.A., Sunkin, S.M., Oh, S.W., Zariwala, H.A., Gu, H., Ng, L.L., Palmiter, R.D., Hawrylycz, M.J., Jones, A.R., et al. (2010). A robust and high-throughput Cre reporting and characterization system for the whole mouse brain. *Nat. Neurosci.* *13*, 133–140.
- Paul, F., Arkin, Y., Giladi, A., Jaitin, D.A., Kenigsberg, E., Keren-Shaul, H., Winter, D., Lara-Astiaso, D., Gury, M., Weiner, A., et al. (2015). Transcriptional Heterogeneity and Lineage Commitment in Myeloid Progenitors. *Cell* *163*, 1663–1677.
- Picelli, S., Faridani, O.R., Björklund, A.K., Winberg, G., Sagasser, S., and Sandberg, R. (2014). Full-length RNA-seq from single cells using Smart-seq2. *Nat. Protoc.* *9*, 171–181.
- Sathe, P., Metcalf, D., Vremec, D., Naik, S.H., Langdon, W.Y., Huntington, N.D., Wu, L., and Shortman, K. (2014). Lymphoid tissue and plasmacytoid dendritic cells and macrophages do not share a common macrophage-dendritic cell-restricted progenitor. *Immunity* *41*, 104–115.
- Schlitzer, A., Sivakamasundari, V., Chen, J., Sumatoh, H.R., Schreuder, J., Lum, J., Malleret, B., Zhang, S., Larbi, A., Zolezzi, F., et al. (2015). Identification of cDC1- and cDC2-committed DC progenitors reveals early lineage priming at the common DC progenitor stage in the bone marrow. *Nat. Immunol.* *16*, 718–728.
- Schulz, C., Gomez Perdiguero, E., Chorro, L., Szabo-Rogers, H., Cagnard, N., Kierdorf, K., Prinz, M., Wu, B., Jacobsen, S.E., Pollard, J.W., et al. (2012). A lineage of myeloid cells independent of Myb and hematopoietic stem cells. *Science* *336*, 86–90.
- Tamoutounour, S., Guillemins, M., Montanana Sanchis, F., Liu, H., Terhorst, D., Malosse, C., Pollet, E., Ardouin, L., Lucche, H., Sanchez, C., et al. (2013). Origins and functional specialization of macrophages and of conventional and monocyte-derived dendritic cells in mouse skin. *Immunity* *39*, 925–938.
- Terry, R.L., and Miller, S.D. (2014). Molecular control of monocyte development. *Cell. Immunol.* *297*, 16–21.
- van Furth, R., and Cohn, Z.A. (1968). The origin and kinetics of mononuclear phagocytes. *J. Exp. Med.* *128*, 415–435.
- Wu, C., Orozco, C., Boyer, J., Leglise, M., Goodale, J., Batalov, S., Hodge, C.L., Haase, J., Janes, J., Huss, J.W., 3rd, and Su, A.I. (2009). BioGPS: an extensible and customizable portal for querying and organizing gene annotation resources. *Genome Biol.* *10*, R130.
- Yanez, A., Coetzee, S.G., Olsson, A., Muench, D.E., Berman, B.P., Hazelett, D.J., Salomonis, N., Grimes, H.L., and Goodridge, H.S. (2017). Granulocyte-Monocyte Progenitors and Monocyte-Dendritic Cell Progenitors Independently Produce Functionally Distinct Monocytes. *Immunity* *47*, 890–902.e4.
- Yona, S., Kim, K.W., Wolf, Y., Mildner, A., Varol, D., Breker, M., Strauss-Ayali, D., Viukov, S., Guillemins, M., Misharin, A., et al. (2013). Fate mapping reveals origins and dynamics of monocytes and tissue macrophages under homeostasis. *Immunity* *38*, 79–91.

STAR★METHODS

KEY RESOURCES TABLE

REAGENT or RESOURCE	SOURCE	IDENTIFIER
Antibodies		
Anti-mouse CD3e APC (145-2C11)	Biolegend	Cat# 100312; RRID: AB_312677
Anti-mouse CD3e APC-efluo780 (145-2C11)	eBioscience	Cat# 47-0031-82; RRID: AB_11149861
Anti-mouse CD4 BV510 (RM4-5)	Biolegend	Cat# 100559; RRID: AB_2562608
Anti-mouse CD8a PE-Cy7 (53-6.7)	eBioscience	Cat# 25-0081-82; RRID: AB_469584
Anti-mouse CD11b APC (M1/70)	Biolegend	Cat# 101212; RRID: AB_312795
Anti-mouse CD11b BV650 (M1/70)	Biolegend	Cat# 101259; RRID: AB_2566568
Anti-mouse CD11c APC (N418)	Biolegend	Cat# 117310; RRID: AB_313779
Anti-mouse CD11c BV510 (N418)	Biolegend	Cat# 117353; RRID: AB_2686978
Anti-mouse CD16/32 APC-Cy7 (93)	Biolegend	Cat# 101328; RRID: AB_2104158
Anti-mouse CD19 APC (eBio1D3)	eBioscience	Cat# 17-0193-82; RRID: AB_1659676
Anti-mouse CD19 eFluor450 (eBio1D3)	eBioscience	Cat# 48-0193-82; RRID: AB_2043815
Anti-mouse CD24 FITC (M1/69)	eBioscience	Cat# 11-0242-81; RRID: AB_464987
Anti-mouse CD26 PE-Cy7 (H194-112)	Biolegend	Cat# 137809; RRID: AB_2564311
Anti-mouse CD34 BV421 (SA376A4)	Biolegend	Cat# 152208; RRID: AB_2650766
Anti-mouse CD45 APC-Cy7 (30-F11)	BD	Cat# 557659; RRID: AB_396774
Anti-mouse CD45 BUUV395 (30-F11)	BD	Cat# 565967; RRID: AB_2739420
Anti-mouse CD45.1 FITC (A20)	eBioscience	Cat# 11-0453-82; RRID: AB_465058
Anti-mouse CD45.2 BUUV395 (104)	BD	Cat# 564616; RRID: AB_2738867
Anti-mouse CD49b APC (DX5)	Biolegend	Cat# 108910; RRID: AB_313417
Anti-mouse CD64 APC (X54-5/7.1)	biolegend	Cat# 139306; RRID: AB_11219391
Anti-mouse CD64 BV421 (X54-5/7.1)	Biolegend	Cat# 139309; RRID: AB_2562694
Anti-mouse CD64 BV711 (X54-5/7.1)	Biolegend	Cat# 139311; RRID: AB_2563846
Anti-mouse CD115 BV605 (AFS98)	Biolegend	Cat# 135517; RRID: AB_2562760
Anti-mouse CD117 BV510 (2B8)	Biolegend	Cat# 105839; RRID: AB_2629798
Anti-mouse CD127 PerCP/Cy5.5 (A7R34)	eBioscience	Cat# 45-1271-82; RRID: AB_1106998
Anti-mouse CD135 biotin (A2F10)	eBioscience	Cat# 13-1351-82; RRID: AB_466599
Anti-mouse CD172a PerCP-eFluor 710 (P84)	eBioscience	Cat# 46-1721-82; RRID: AB_10804639
Anti-mouse CD326 FITC (G8.8)	eBioscience	Cat# 11-5791-80; RRID: AB_11151327
Anti-mouse F4/80 Alexa Fluor 488 (BM8)	Biolegend	Cat# 123119; RRID: AB_893491
Anti-mouse F4/80 BV605 (BM8)	Biolegend	Cat# 123133; RRID: AB_2562305
Anti-mouse F4/80 PE-Cy7 (BM8)	Biolegend	Cat# 123113; RRID: AB_893490
Anti-mouse F4/80 biotin	eBioscience	Cat# 13-4801-81; RRID: AB_466656
Anti-mouse FceRI PE (MAR-1)	Biolegend	Cat# 134307; RRID: AB_1626104
Anti-mouse FceRI PE-Cy7 (MAR-1)	eBioscience	Cat# 25-5898-80; RRID: AB_2573492
Anti-mouse Gr-1 APC (RB6-8C5)	eBioscience	Cat# 17-5931-82; RRID: AB_469476
Anti-mouse Ly6C Alexa Fluor 488 (HK1.4)	Biolegend	Cat# 128022; RRID: AB_10639728
Anti-mouse Ly6C BV785 (HK1.4)	Biolegend	Cat# 128041; RRID: AB_2565852
Anti-mouse Ly6G APC (1A8)	Biolegend	Cat# 127614; RRID: AB_2227348
Anti-mouse Ly6G BV711 (1A8)	Biolegend	Cat# 127643; RRID: AB_2565971
Anti-mouse Ly6A/E (Sca-1) Alexa Fluor 700 (D7)	eBioscience	Cat# 56-5981-82; RRID: AB_657836
Anti-mouse MHCII (I-A/I-E) Alexa Fluor 700 (M5/114.15.2)	eBioscience	Cat# 56-5321-82; RRID: AB_494009
Anti-mouse MHCII (I-A/I-E) APC (M5/114.15.2)	eBioscience	Cat# 17-5321-82; RRID: AB_469455
Anti-mouse NK1.1 FITC (PK136)	eBioscience	Cat# 11-5941-82; RRID: AB_465318
Anti-mouse Siglec F Alexa Fluor 647 (E50-2440)	BD	Cat# 562680; RRID: AB_2687570

(Continued on next page)

Continued

REAGENT or RESOURCE	SOURCE	IDENTIFIER
Anti-mouse Siglec F BV421 (E50-2440)	BD	Cat# 562681; RRID: AB_2722581
Anti-mouse Ter-119 APC (TER-119)	Biolegend	Cat# 116212; RRID: AB_313713
Anti-mouse TIM-4 Alexa Fluor 647 (RMT4-54)	Biolegend	Cat# 130008; RRID: AB_2271648
Anti-mouse TIM-4 PerCP-eFluor 710 (RMT4-54)	eBioscience	Cat# 46-5866-80; RRID: AB_2573780
Anti-mouse XCR1 BV650 (ZET)	Biolegend	Cat# 148220; RRID: AB_2566410
Streptavidin PE-Cy7	eBioscience	Cat# 25-4317-82; RRID: AB_10116480
Streptavidin BV737	BD	Cat# 564293
Anti-mouse IL-4 (11B11) purified	BioXcell	Cat# BP0045
Chemicals, Peptides, and Recombinant Proteins		
Collagenase type IV	Sigma	Cat# C5138
DNase I	Roche	Cat# 1 0104159 001
Dispase	GIBCO	Cat# 17105-041
LPS-EB VacchiGrade	InvivoGen	Cat# vac-3pelps
CpG	InvivoGen	Cat# ODN 1826
Thioglycollate Medium Brewer Modified	BD	REF# 211716
DAPI	ThermoFisher	Cat# D1306
Recombinant mouse IL-4	peprotech	Cat# 214-14
Clodronate Liposomes	Yeasen	Cat# 40337ES10
Control Liposomes (PBS)	Yeasen	Cat# 40338ES10
Tamoxifen	Sigma	Cat# T5648
Trizol reagent	ThermoFisher	Cat# 15596026
GlycoBlue Coprecipitant	ThermoFisher	Cat# AM9515
Critical Commercial Assays		
SuperScript II Reverse Transcriptase	ThermoFisher	Cat# 18064014
Power SYBR Green PCR Master Mix	ThermoFisher	Cat# 4367659
Direct Lineage Cell Depletion Kit	Miltenyi	Cat# 130-110-470
Deposited Data		
scRNA-seq data of monocyte/DC progenitors	This paper	GEO: GSE60783
Bulk mRNA-seq data	This paper	NCBI BioProject SRA: PRJNA555467
Experimental Models: Organisms/Strains		
Mouse: <i>Rosa26^{tdTomato}</i>	Madisen et al., 2010	JAX 007914
Mouse: <i>Ms4a3^{Cre}</i>	This paper	N/A
Mouse: <i>Ms4a3^{tdTomato}</i>	This paper	N/A
Mouse: <i>Ms4a3^{CreERT2}</i>	This paper	N/A
Mouse: <i>Cx3cr1^{gfp}</i>	Jung et al., 2000	JAX 005582
Mouse: <i>Cx3cr1^{Cre}</i>	Yona et al., 2013	JAX 025524
Oligonucleotides		
qPCR primer sequences	This paper	See Method Details
Genotyping primer sequences	This paper	See Method Details
Software and Algorithms		
FlowJo V10	FlowJo	https://www.flowjo.com
GraphPad Prism 6	GraphPad Software	https://www.graphpad.com
Imaris	Bitplane	https://imaris.oxinst.com

LEAD CONTACT AND MATERIALS AVAILABILITY

Further information and requests for resources and reagents should be directed to and will be fulfilled by the Lead Contact, Florent Ginhoux (florent_ginhoux@immunol.a-star.edu.sg).

EXPERIMENTAL MODEL AND SUBJECT DETAILS

Animals

Ms4a3^{TdT}, *Ms4a3^{Cre}* and *Ms4a3^{CreERT2}* mice were generated at the Shanghai Model Organisms Center, Inc. Briefly, an *Ires-tdTomato* or *Ires-Cre* or *Ires-CreERT2* gene fusion was inserted into the 3' un-translated region (3'UTR) of the *Ms4a3* gene by CRISPR-Cas9 technique in C57BL/6 zygotes (*Ms4a3^{TdT}* and *Ms4a3^{Cre}*) or by homologous recombination in ES cells (*Ms4a3^{CreERT2}*). To eliminate off-target effects, knock-in mice were then backcrossed onto a C57BL/6 background for three generations. All these three mouse strains were genotyped by PCR using the following primers:

Common forward primer 5'- AGAGAAATCATCAGGGCAGAAAT -3';
 Mutant reverse primer 5'- TTGGCGAGAGGGGAAAGAC -3' (412 bp fragment);
 Wild-type reverse primer 5'-GAAAGGGGAACAAGCGAAGAT-3' (517 bp fragment).

Rosa26^{tdTomato} reporter mice have been previously described (Madisen et al., 2010). *Cx3cr1^{gfp}*, *Cx3cr1^{Cre}* and *Cx3cr1^{CreERT2}* mice have been previously described (Jung et al., 2000; Yona et al., 2013). All mice were bred in a specific pathogen-free animal facility at the Shanghai Jiao Tong University School of Medicine. All animal experiments were approved by the Institutional Animal Care and Use Committee (IACUC) of Shanghai Jiao Tong University School of Medicine and were performed in compliance with the University's guidelines for the care and use of laboratory animals.

METHOD DETAILS

Single cell RNA-sequencing (scRNA-seq)

Cell populations (blood Ly6C^{hi} monocytes, BM Ly6C⁺ monocytes and BM cMoPs) were isolated by FACS and diluted to a final concentration range of 250–400 cells/μl. The cells were then loaded onto C1 integrated fluidic circuits (5–10-μm chip) for cell lysis, reverse transcription with oligo (dT) primers and cDNA amplification on a C1 Single-cell Auto Prep System, according to the manufacturer's mRNA-seq protocol (Fluidigm). Array control RNA spikes were used (1, 4 and 7) (PN AM1781) according to the manufacturer's protocol (Ambion). The cDNA generated from single cells was quantified with a QuantiT PicoGreen dsDNA Assay Kit (PN P11496; Life Technologies), and the quality was checked using High Sensitivity DNA Reagents (PN 5067-4626), according to the manufacturer's instructions (Agilent Technologies). Only cells with high-quality cDNA were processed for subsequent library preparation. A Nextera XT Kit (PN FC-131-1096; Illumina) with dual indices (PN FC-131-1002; Illumina) was used to prepare single-cell multiplexed libraries, which were sequenced as 51-bp single-end reads on an Illumina HiSeq 2000 platform. Single-end reads were mapped to the mm9 reference genome (NCBI assembly of the mouse genome).

scRNA-seq data analysis

CMap analysis is an extension of the GSEA algorithm (provided by the Broad Institute) in which 'enrichment' of a gene set (signature genes) in another gene set can be measured. CMap scores are scaled, dimensionless quantities that indicate the degree of enrichment or 'closeness' of one assessed cell subset to another. Monocyte and DC signature genes were identified from both the literature and our transcriptomic data, and were used as signature genes for the respective populations for CMap analysis of each single cell. The 'enrichment' of gene sets was tested with 1,000 permutations. Cells with a gene-expression profile that significantly correlated with signature genes were selected by a P value of < 0.05 after 1,000 permutations. CMap scores were scaled to a range of -1 to 1. Cells with a positive CMap score were denoted as monocytes or monocyte primed cells, while cells with a negative CMap score were denoted as DCs or DC-primed cells. DEGs between monocyte-primed progenitors versus DC-primed progenitors at the BM MDP, CD115⁺ CDP, pre-DC and cMoP stages were identified using the Seurat R package. The bimodal likelihood-ratio test for single cell gene expression was used for DEG analysis, and genes with adjusted p values < 0.05 were identified as being differentially expressed.

Quantitative Real-Time PCR (qRT-PCR)

Total RNA was isolated from sorted cells using TRIzol reagent (Invitrogen), according to the manufacturer's protocol. Glycoblue (Invitrogen) was added as a co-precipitant when handling < 10⁶ cells. cDNA was synthesized using an M-MLV First-Strand Synthesis Kit (Invitrogen, C28025-021) with oligo (dT) primers. qRT-PCR was performed using FastStart Universal SYBR Green Master with Rox (Applied Biosystems) on a ViiA 7 Real-Time PCR system (Applied Biosystems). The following primers were used for qRT-PCR:

Ms4a3 forward primer 5'- GTGGTTCTGTTTATCAGCCCTT-3';
Ms4a3 reverse primer 5'- ACAGTGGGTAGCCTGTGTAGA-3';
tdTomato forward primer 5'- CCTGTTCCCTGGGGCATGG-3';
tdTomato reverse primer 5'- TGATGACGGCCATGTTGTTG-3';
Gapdh forward primer 5'- AGGTCGGTGTGAACGGATTTG-3';
Gapdh reverse primer 5'- TGTAGCCATGTAGTTGAGGTCA-3'.

All data were normalized to *Gapdh* quantified in parallel amplification reactions.

Tissue preparation for flow cytometry

Blood was collected by cardiac puncture from terminally anaesthetized mice; the mice were then euthanized by cervical dislocation. Peritoneal lavage was obtained by injecting 5 mL PBS containing 2 mM EDTA into the peritoneal cavity, and the washout was collected. The mice were then perfused with PBS via the left ventricle. The spleen was harvested and homogenized into a single-cell suspension using a 70 μ m cell strainer and syringe plungers, then lysed in ACK lysis buffer (155 mM NH₄Cl, 10 mM KHCO₃, 0.1 mM EDTA) and again passed through a 70 μ m cell strainer.

To obtain microglia, the brain was cut into small pieces and digested with 0.2 mg/mL collagenase type IV (C5138, Sigma) and 0.05 mg/mL DNase I (Roche) in RPM1640 medium with 10% FCS at 37°C for 60 min. The digested suspension was homogenized with a syringe with a 1.2 mm inner diameter needle. The brain-cell suspension was separated by 40%/80% layered Percoll (GE Healthcare) gradient centrifugation at 1,578 x g for 20 min at room temperature with low acceleration and no brake. The middle interface layer was collected. For newborn mice, the digested brain suspension was used for staining without Percoll separation.

For skin preparation (Tamoutounour et al., 2013), ears were split between the dorsal and ventral sections, and digested in dispase solution (GIBCO) at 37°C for 90 min. The dermis and epidermis were separated and further digested as described for brain tissues. The dermis and epidermis were disrupted into single-cell suspensions using a syringe with a 1.2 mm inner diameter needle and passed through a 70 μ m cell strainer.

For adult lung, liver and kidney tissues and newborn mouse tissues, tissues were cut into small pieces and digested and homogenized as described for brain preparations. Red blood cells were lysed in ACK lysis buffer.

For intestine preparation (Bain et al., 2014), the colon and small intestine were removed and washed in PBS, and the fat tissue and Peyer's patches in the small intestine were removed. The intestines were opened longitudinally, cut into 0.5 cm sections and washed four times with PBS. After washing, 12.5 mL fresh calcium/magnesium-free PBS containing 5 mM EDTA and 2 mM DTT was added and the tube was incubated at 37°C with agitation for 20 min to detach the epithelial cells. The epithelial sheet was removed by vigorous shaking and the remaining tissue was washed twice with PBS, cut into small pieces and then digested and homogenized as described for brain preparations.

Flow Cytometry

For BM progenitor analysis, BM cells were stained with APC-Cy7 conjugated anti-CD16/32 (clone 93; Biolegend) at 4°C for 15 min, and then stained with other antibodies at 4°C for 25 min. Antibodies used for flow cytometry can be found in the [Key Resources Table](#). PE-Cy7-conjugated streptavidin was used to detect biotin-labeled CD135 (clone A2F10; eBioscience). Lineage markers used in the BM progenitor analysis included CD3e, CD19, CD49b, Ly6G, Ter-119, B220, CD11c and CD11b. For flow cytometry of other samples, nonspecific antibody binding to cells was blocked by incubation with an anti-CD16/32 antibody (clone 2G8; BD Biosciences) at 4°C for 15 min, and the cells were stained with fluorophore-conjugated or biotin-conjugated antibodies at 4°C for 25 min. Cells were maintained at 4°C and analyzed on a BD Fortessa X20 or Symphony (BD Biosciences). Data were analyzed in FlowJo (FlowJo LLC). tSNE analysis was calculated with all the markers used for flow cytometry, except tdTomato.

Cell Sorting

For peripheral blood, splenic DC and RTM cell sorting, nonspecific antibody binding to cells was blocked by incubating cells with an anti-CD16/32 antibody (clone 2.4G2; BD Biosciences) at 4°C for 15 min. The cells were then stained with fluorophore-conjugated antibodies ([Key Resources Table](#)) at 4°C for 25 min. FACS was performed on a BD FACS Aria III (BD Biosciences) to achieve > 95% purity. Dead cells were excluded by DAPI (Invitrogen) staining.

For BM progenitor cell sorting, BM cells from the tibia and femur were used and lineage cells were depleted with a Direct Lineage Depletion Kit (Lin: CD5, CD11b, CD45R [B220], Anti-Gr-1 [Ly-6G/C], 7-4, and Ter-119; Miltenyi). Lin⁻ cells were stained with APC-Cy7 conjugated with an anti-CD16/32 antibody and incubated at 4°C for 15 min before staining with other antibodies and secondary PE-Cy7 conjugated streptavidin at 4°C for 25 min. FACS was performed on a BD FACS Aria III (BD Biosciences) to achieve > 95% purity.

In vitro culture

Indicated BM progenitor cells were sorted from pooled BM of CD45.2 *Ms4a3^{Cre}-Rosa^{TdT}* mice and mixed with 500,000 BM cells from CD45.1 mice, and cultured *in vitro* in media (RPMI with 10% FCS and 1% penicillin-streptomycin) supplemented with M-CSF (50 ng/mL; Peprotech). Cells were harvested and analyzed by flow cytometry at the indicated time point.

In vivo transfer

Indicated BM progenitor cells were sorted from pooled BM of *Ms4a3^{Cre}-Rosa^{TdT}* (CD45.2 background) mice. Progenitor cells were intravenously or intra-bone marrow transferred into non-irradiated CD45.1 recipient mice (10,000-20,000 cells/mouse). Donor derived cells in the BM (femurs and tibias), spleen and blood were analyzed at the indicated time point.

Confocal microscopy

Tissues were harvested and fixed overnight in fixation buffer containing 1% PFA. The tissues were then dehydrated in 30% sucrose before embedding in OCT freezing media (Sakura). Sections were cut to 10- μ m on a Leica cryostat and blocked for 1 h at room temperature in blocking buffer containing 1% normal mouse serum, 1% BSA and 0.3% Triton X-100. The sections were stained with the

indicated fluorophore-conjugated antibodies overnight at 4°C in a dark, humidified chamber. Antibodies for immunofluorescence can be found in the [Key Resources Table](#). Images were captured under a Leica TCS SP8 laser confocal microscope (Leica).

Tamoxifen induction

Tamoxifen was prepared by dissolving in corn oil for a final concentration of 17.5 mg/mL and stored at –20°C. Adult *Ms4a3^{CreERT2}-Rosa^{TdT}* and *Cx3cr1^{CreERT2}-Rosa^{TdT}* mice were given 100 µL (1.75 mg) tamoxifen solution once a day for 4 days by i.p. injection or by gavage as indicated.

Inflammatory models

For thioglycollate-induced sterile peritonitis, 1 mL of 4% sterile thioglycollate broth (BD Biosciences) was injected i.p. into 8-week-old female mice and then analyzed at the indicated time points. For long-acting IL-4 treatment, a mix of 5 µg recombinant mouse IL-4 (Peprotech) and 25 µg anti-IL-4 mAb (clone 11B11; BioXcell, NH) was incubated for 5 min on ice to form an IL-4:anti-IL-4 complex (IL-4c). IL-4c enables sustained and slow IL-4 release. Mice were then injected i.p. with IL-4c (containing 5 µg IL-4 and 25 µg anti-IL4), or PBS vehicle control on days 0 and 2. The peritoneal lavage was analyzed at the indicated time points. For LPS-induced peritonitis, 50 µg sterile LPS (InvivoGen) was injected i.p. and peritoneal lavage was analyzed at the indicated time points. For LPS and CpG-induced lung inflammation models, lightly anesthetized mice with isoflurane were instilled i.n. with 50 µL saline (vehicle control) or 50 µL saline containing 10 µg LPS (InvivoGen) or 50 µg CpG (InvivoGen). Mice were then analyzed at the indicated time points.

Bulk RNA Sequencing

Peritoneal macrophages and monocytes were sorted from control and thioglycollate treated mice at different time points. Total RNA was isolated from sorted cells using TRIzol reagent (Invitrogen), according to the manufacturer's protocol. Total RNA was reverse transcribed with the SMART-seq2 protocol (Picelli et al., 2014). Samples were sequenced on an Illumina NextSeq 500 sequencer using pair-end 75 base pair reading. Sequencing data were aligned to the mouse reference genome (version mm10).

Macrophage depletion with clodronate liposome

Mice were injected i.v. with 200 µL clodronate liposome (Yeasen) or empty liposome control to deplete RTMs in the spleen. Tissues were harvested at the indicated time points for flow cytometry.

QUANTIFICATION AND STATISTICAL ANALYSIS

Statistical analysis

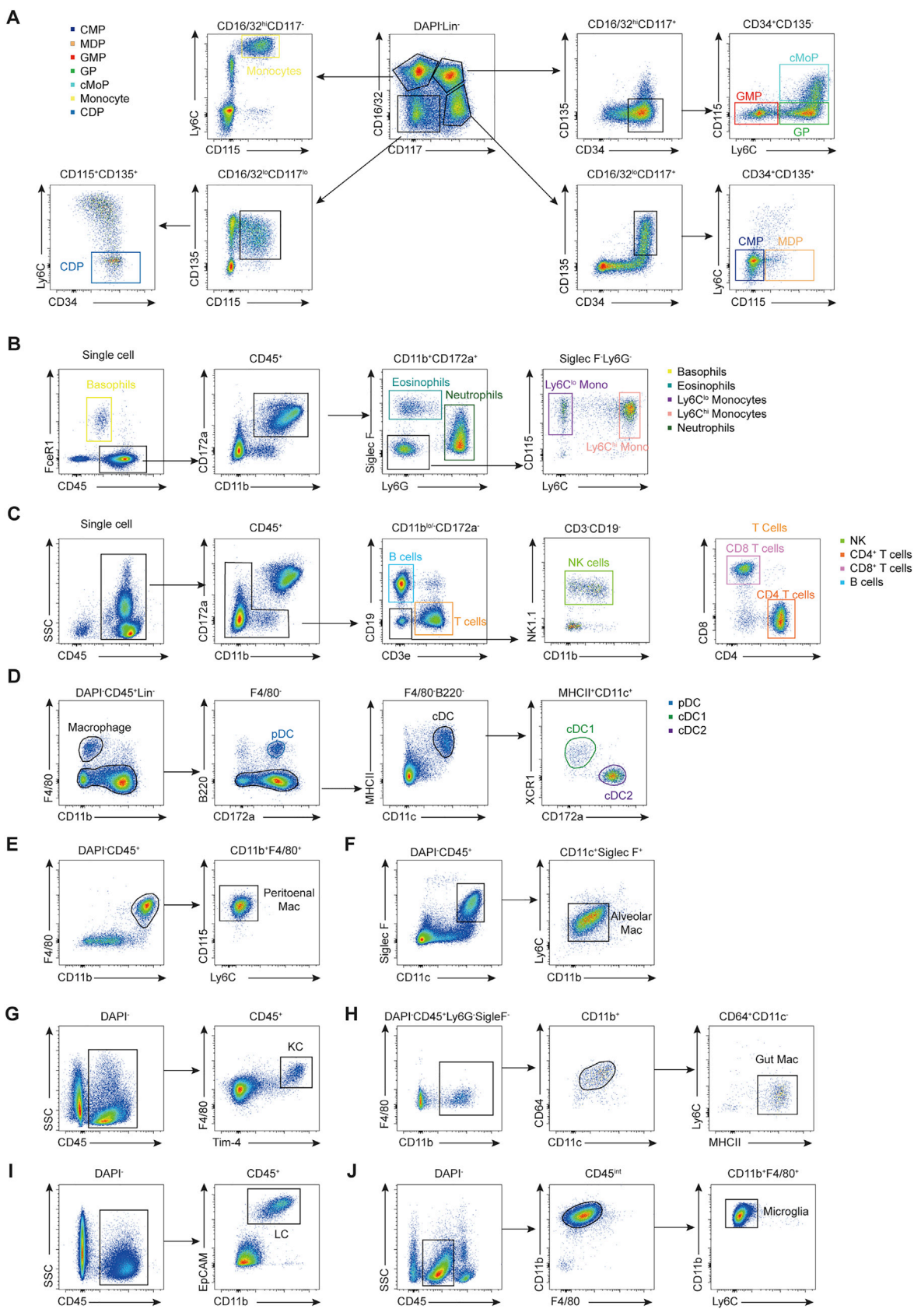
The statistical analyses performed for each experiment are indicated in the figure legends. No statistical methods were used to pre-determine the sample size. The experiments were not randomized. The investigators were not blinded to allocation during experiments and outcome assessment.

DATA AND CODE AVAILABILITY

The scRNA-seq dataset is deposited in the Genome Expression Omnibus under accession number GEO: GSE134523. The bulk RNA-seq data is deposited in the Sequence Read Archive (SRA) under accession number SRA: PRJNA555467.

Figure S1. Ms4a3 Is Specifically Expressed by Monocyte-Committed Progenitors, Related to Figure 1

- (A) scRNA-seq workflow of BM cMoPs, BM monocytes and blood monocytes using Fluidigm C1 autoprep system.
- (B) Sorting panel for blood Ly6C^{hi} monocytes.
- (C) Sorting panel for BM cMoPs and BM Ly6C⁺ monocytes. Lineage markers include CD3e, CD19, CD49b, Ly6G.
- (D) Heatmap generated with the top 10 DEGs for each population.
- (E) Ms4a3 expression profile in BM progenitors using ImmGen dataset.
- (F) Ms4a3 expression profile in DCs and RTM populations using ImmGen dataset.
- (G) Ms4a3 expression profile using BioGPS dataset.



(legend on next page)

Figure S2. SORTING PANEL for Indicated Cell Populations, Related to Figure 1

(A) Sorting panel for BM CMPs, GMPs, GPs, cMoPs, Ly6C⁺ monocytes, MDPs and CDPs. BM CMPs were defined as Lin⁻Sca-1⁻CD117⁺CD16/32^{lo}CD34⁺CD135⁺CD115⁻; GMPs as Lin⁻Sca-1⁻CD117⁺CD16/32^{hi}CD34⁺CD135⁻Ly6C⁻; GPs as Lin⁻Sca-1⁻CD117⁺CD16/32^{hi}CD34⁺CD135⁻Ly6C⁺CD115⁻; cMoPs as Lin⁻Sca-1⁻CD117⁺CD16/32^{hi}CD34⁺CD135⁻Ly6C⁺CD115⁺; BM monocytes as Lin⁻Sca-1⁻CD117⁻CD16/32^{hi}CD34⁻CD135⁻Ly6C⁺CD115⁺. MDPs as Lin⁻Sca-1⁻CD117⁺CD16/32^{lo}CD34⁺CD135⁺CD115⁺Ly6C⁻; CDPs as Lin⁻Sca-1⁻CD117^{lo}CD16/32^{lo}CD34⁺CD135⁺CD115⁺Ly6C⁻; Lineage markers include CD3e, CD19, CD49b, Ly6G, Ter-119, B220, CD11c and CD11b.

(B) Sorting panel for myeloid lineage cells (basophils, neutrophils, eosinophils, and Ly6C^{hi} and Ly6C^{lo} monocytes) in peripheral blood.

(C) Sorting panel for lymphoid lineage cells (B cells, NK cells, CD4⁺ T cells and CD8⁺ T cells) in peripheral blood.

(D) Sorting panel for splenic cDCs (cDC1 and cDC2) and pDCs.

(E) Sorting panel for peritoneal macrophages.

(F) Sorting panel for lung AMs.

(G) Sorting panel for liver KCs.

(H) Sorting panel for gut macrophages.

(I) Sorting panel for epidermal LCs.

(J) Sorting panel for brain microglia cells.

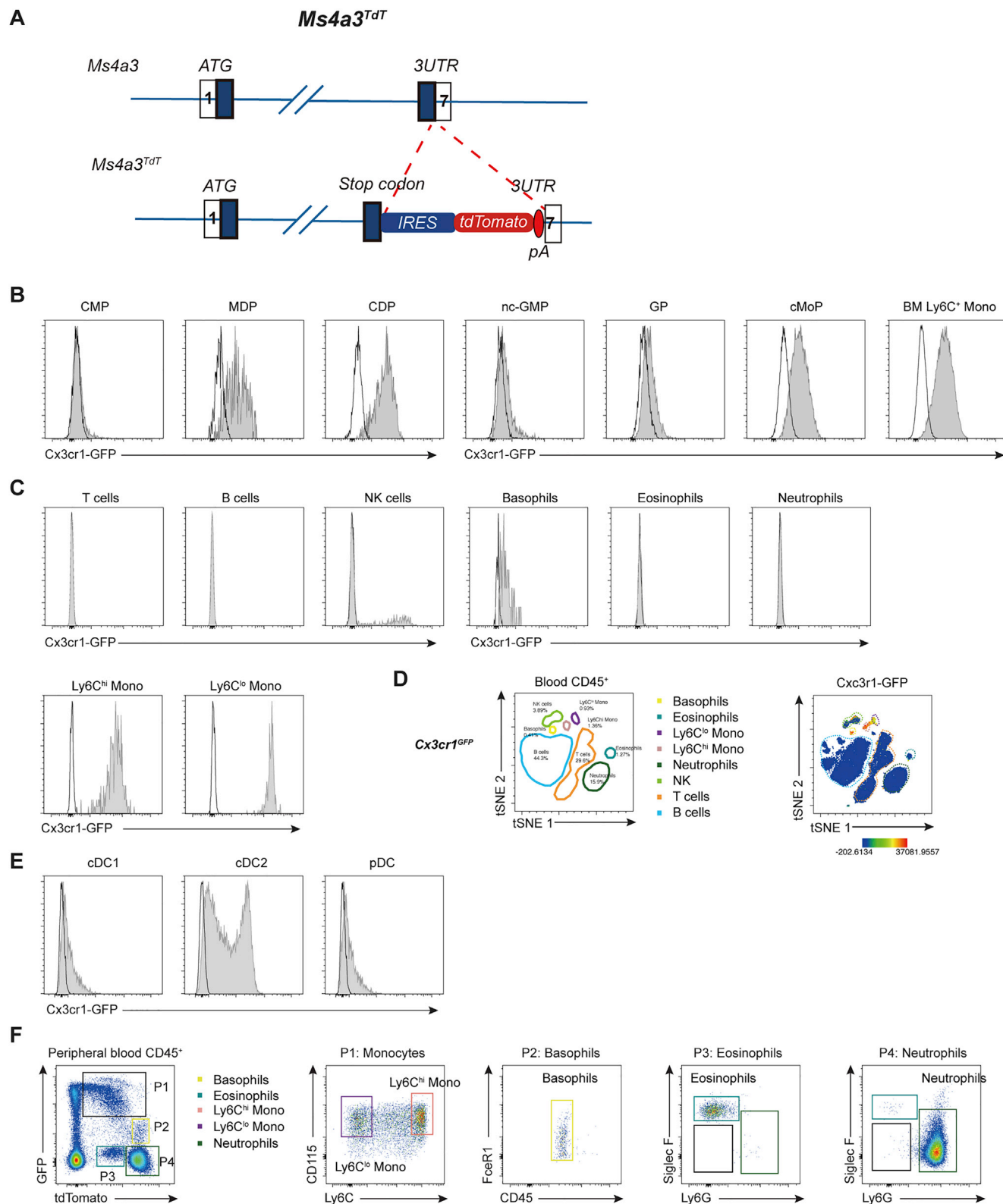


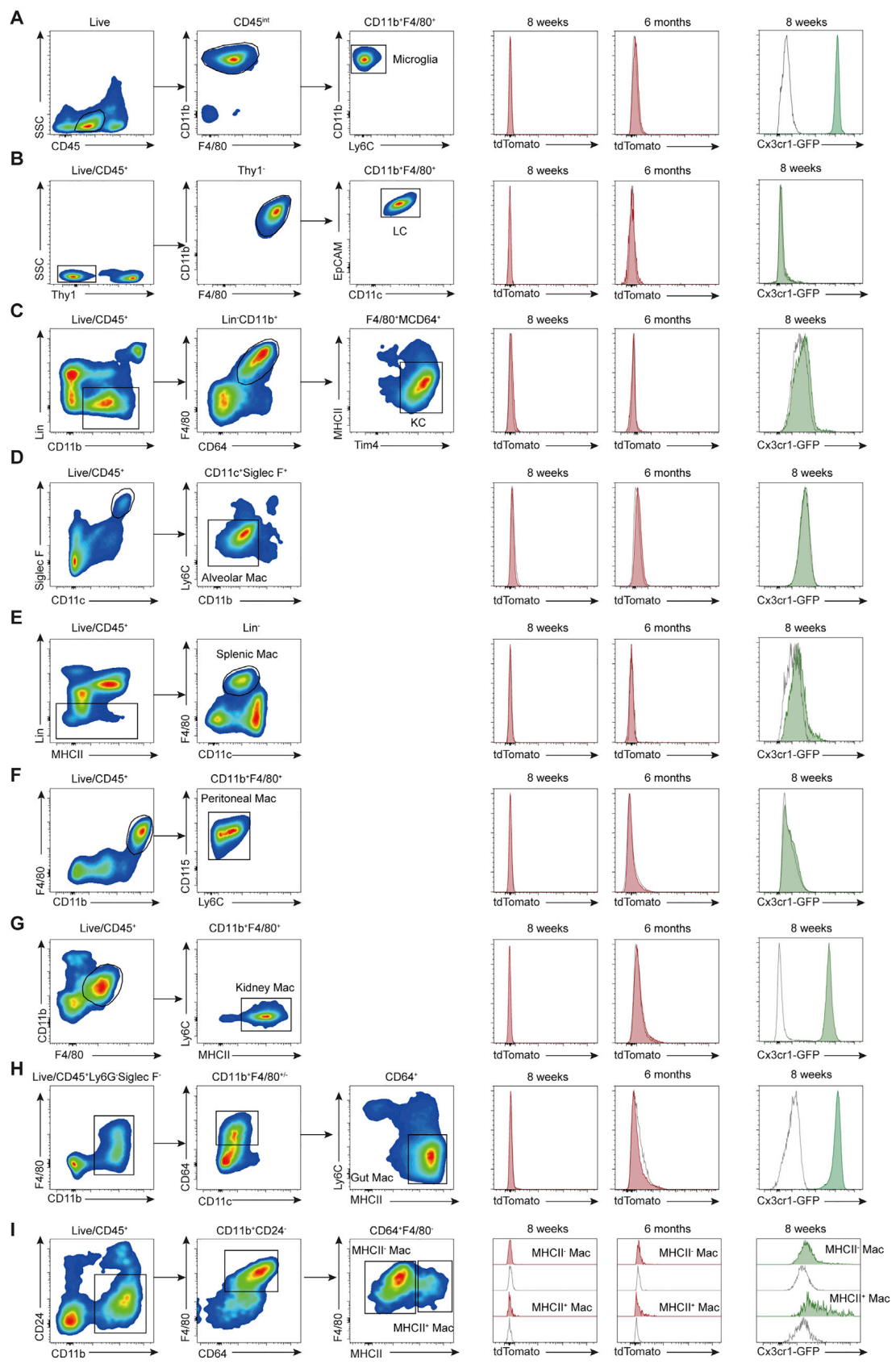
Figure S3. Parallel Comparison of *Ms4a3^{TdT}* and *Cx3cr1^{Gfp}*, Related to Figure 2

(A) Schematic of *Ms4a3^{TdT}* mice. An *Ires-tdTomato-pA* cassette was inserted after the stop codon.

(B) Expression of Cx3cr1-GFP in the indicated BM progenitors in *Cx3cr1^{Gfp}* (filled gray) and WT (open) mice.

(legend continued on next page)

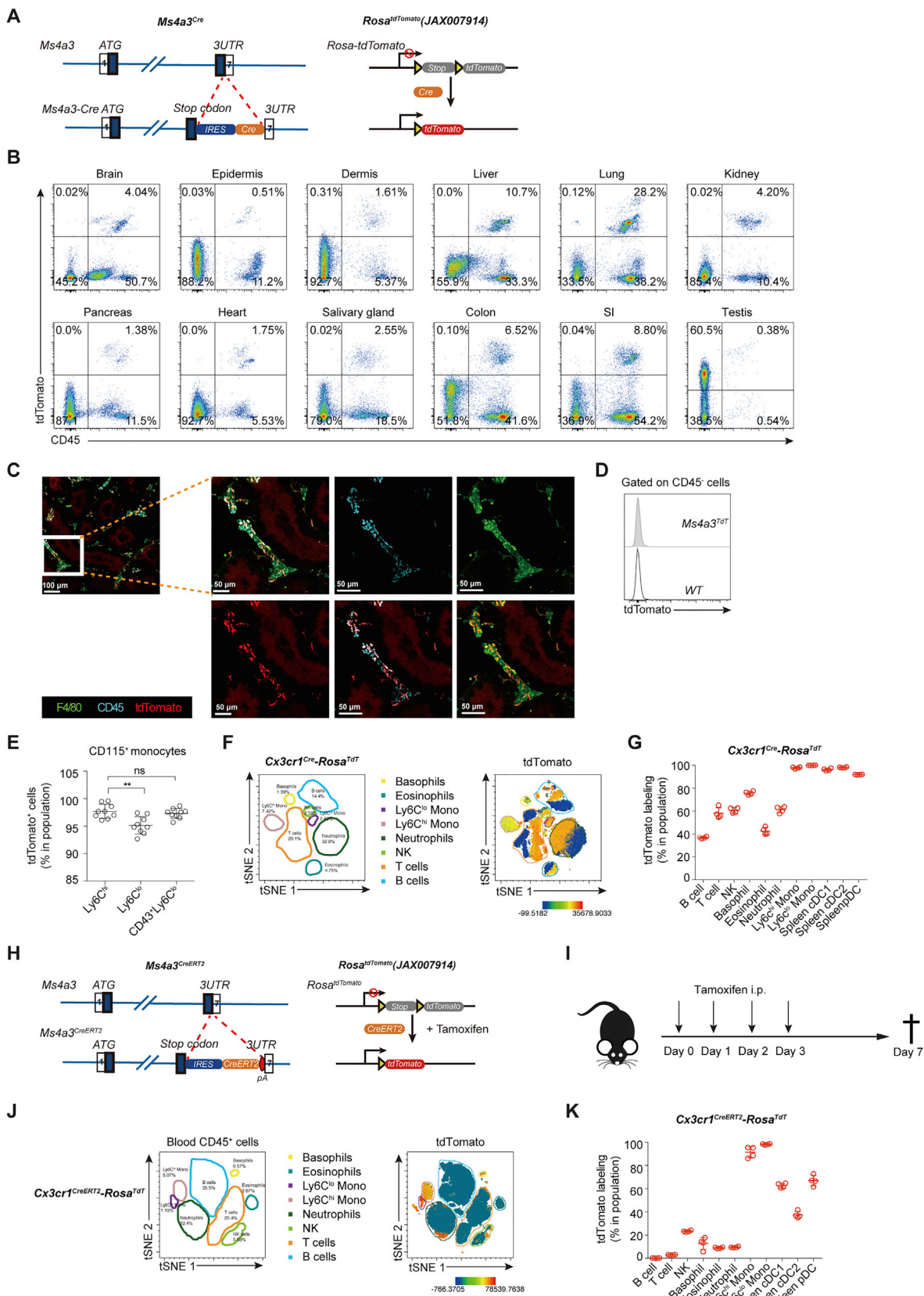
-
- (C) Expression of Cx3cr1-GFP in the indicated cell types in peripheral blood of *Cx3cr1^{gfp}* (filled gray) and WT (open) mice.
- (D) tSNE plot shows the intensity of Cx3cr1-GFP in peripheral blood cells, the color indicates the expression intensity of GFP, red indicates high expression, blue indicates low expression.
- (E) Expression of Cx3cr1-GFP in splenic cDCs and pDCs from *Cx3cr1^{gfp}* (filled gray) and WT (open).
- (F) Flow cytometric analysis of peripheral blood cells of *Cx3cr1^{gfp};Ms4a3^{tdTomato}* mice. Differential expression of Cx3cr1-GFP and Ms4a3-tdTomato could be used to distinguish different myeloid populations.



(legend on next page)

Figure S4. Expression of *Ms4a3*-tdTomato and *Cx3cr1*-GFP in RTMs, Related to Figure 2

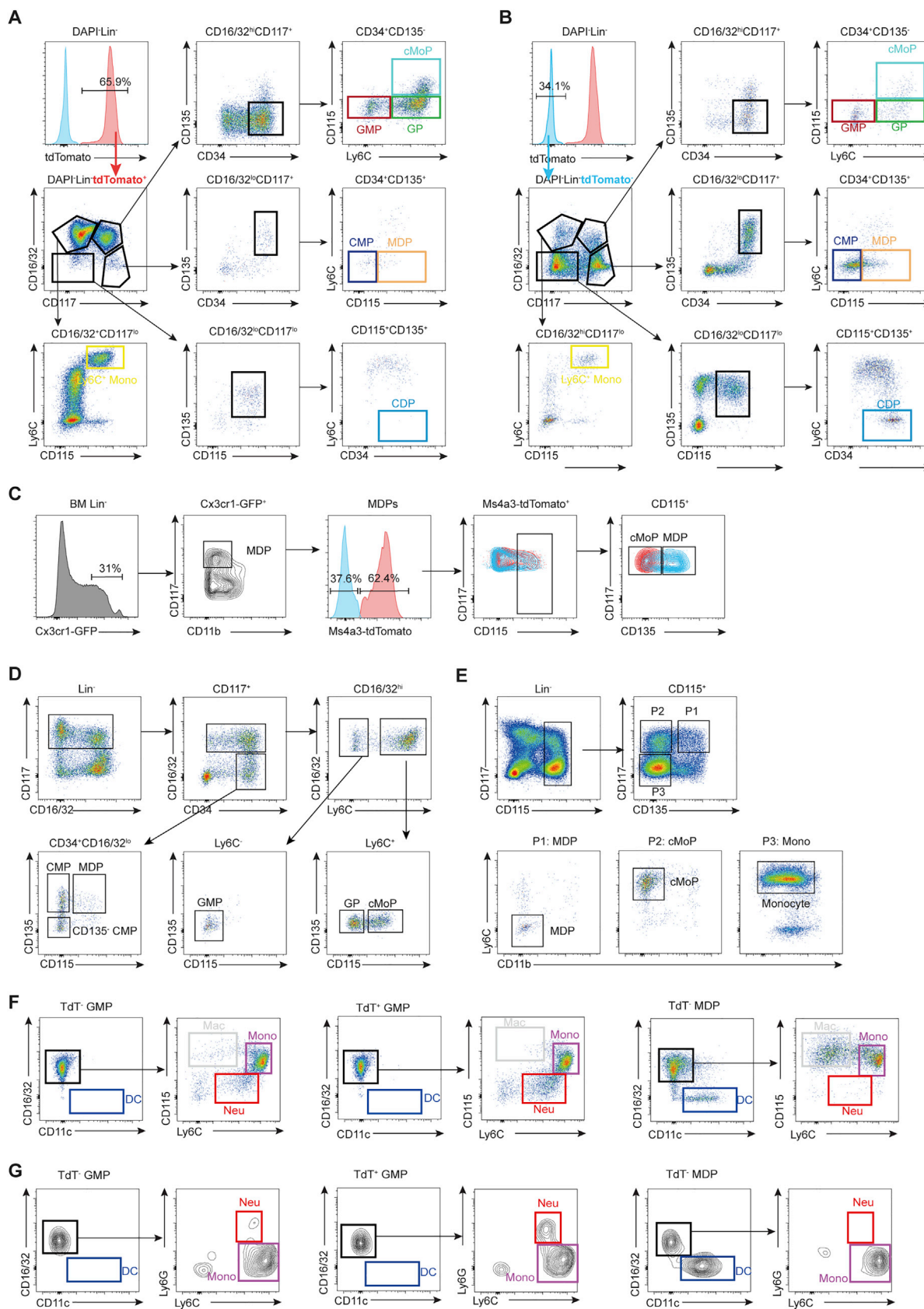
- (A) Gating strategy of brain microglia ($CD45^{int}CD11b^+F4/80^+Ly6C^-$), histogram showing the intensity of tdTomato expression in microglia of 8-week-old and 6-month-old *Ms4a3^{TdT}* (filled red) and WT mice (open), and *Cx3cr1*-GFP expression in 8-week-old *Cx3cr1^{gfp}* (filled green) and WT mice (open).
- (B) Gating strategy of epidermal LCs ($CD45^+Thy1^-CD11b^+F4/80^+EpCAM^+$), histogram showing the intensity of tdTomato expression in LCs of 8-week-old and 6-month-old *Ms4a3^{TdT}* (filled red) and WT mice (open), and *Cx3cr1*-GFP expression in 8-week-old *Cx3cr1^{gfp}* (filled green) and WT mice (open).
- (C) Gating strategy of liver KCs ($CD45^+Lin^-CD11b^+F4/80^+Tim-4^+$), lineage markers include CD3e, CD19, CD49b, Ly6G. Histogram showing the intensity of tdTomato expression in KCs of 8-week-old and 6-month-old *Ms4a3^{TdT}* (filled red) and WT mice (open), and *Cx3cr1*-GFP expression in 8-week-old *Cx3cr1^{gfp}* (filled green) and WT mice (open).
- (D) Gating strategy of AMs ($CD45^+SiglecF^+CD11c^+CD11b^{lo}Ly6C^-$), histogram showing the intensity of tdTomato expression in AMs of 8-week-old and 6-month-old *Ms4a3^{TdT}* (filled red) and WT mice (open), and *Cx3cr1*-GFP expression in 8-week-old *Cx3cr1^{gfp}* (filled green) and WT mice (open).
- (E) Gating strategy of splenic macrophages ($CD45^+Lin^-F4/80^+$), lineage markers include CD3e, CD19, CD49b, Ly6G. Histogram showing the intensity of tdTomato expression in splenic macrophages of 8-week-old and 6-month-old *Ms4a3^{TdT}* (filled red) and WT mice (open), and *Cx3cr1*-GFP expression in 8-week-old *Cx3cr1^{gfp}* (filled green) and WT mice (open).
- (F) Gating strategy of peritoneal macrophages ($CD45^+CD11b^{hi}F4/80^{hi}$), histogram showing the intensity of tdTomato expression in peritoneal macrophages of 8-week-old and 6-month-old *Ms4a3^{TdT}* (filled red) and WT mice (open), and *Cx3cr1*-GFP expression in 8-week-old *Cx3cr1^{gfp}* (filled green) and WT mice (open).
- (G) Gating strategy of kidney macrophages ($CD45^+CD11b^+F4/80^+MHCII^+$), histogram showing the intensity of tdTomato expression in kidney macrophages of 8-week-old and 6-month-old *Ms4a3^{TdT}* (filled red) and WT mice (open), and *Cx3cr1*-GFP expression in 8-week-old *Cx3cr1^{gfp}* (filled green) and WT mice (open).
- (H) Gating strategy of gut macrophages ($CD45^+SiglecF^-Ly6G^-CD11c^-CD11b^+CD64^+Ly6C^-MHCII^+$), histogram showing the intensity of tdTomato expression in gut macrophages of 8-week-old and 6-month-old *Ms4a3^{TdT}* (filled red) and WT mice (open), and *Cx3cr1*-GFP expression in 8-week-old *Cx3cr1^{gfp}* (filled green) and WT mice (open).
- (I) Gating strategy of dermal MHCII⁺ macrophages ($CD45^+CD11b^+F4/80^+CD64^+MHCII^+$) and MHCII⁻ macrophages ($CD45^+CD11b^+F4/80^+CD64^+MHCII^-$), histogram showing the intensity of tdTomato expression in dermal macrophages of 8-week-old and 6-month-old *Ms4a3^{TdT}* (filled red) and WT mice (open), and *Cx3cr1*-GFP expression in 8-week-old *Cx3cr1^{gfp}* (filled green) and WT mice (open).



(legend on next page)

Figure S5. Parallel Comparison of *Ms4a3*-Based and *Cx3cr1*-Based Models, Related to Figure 3

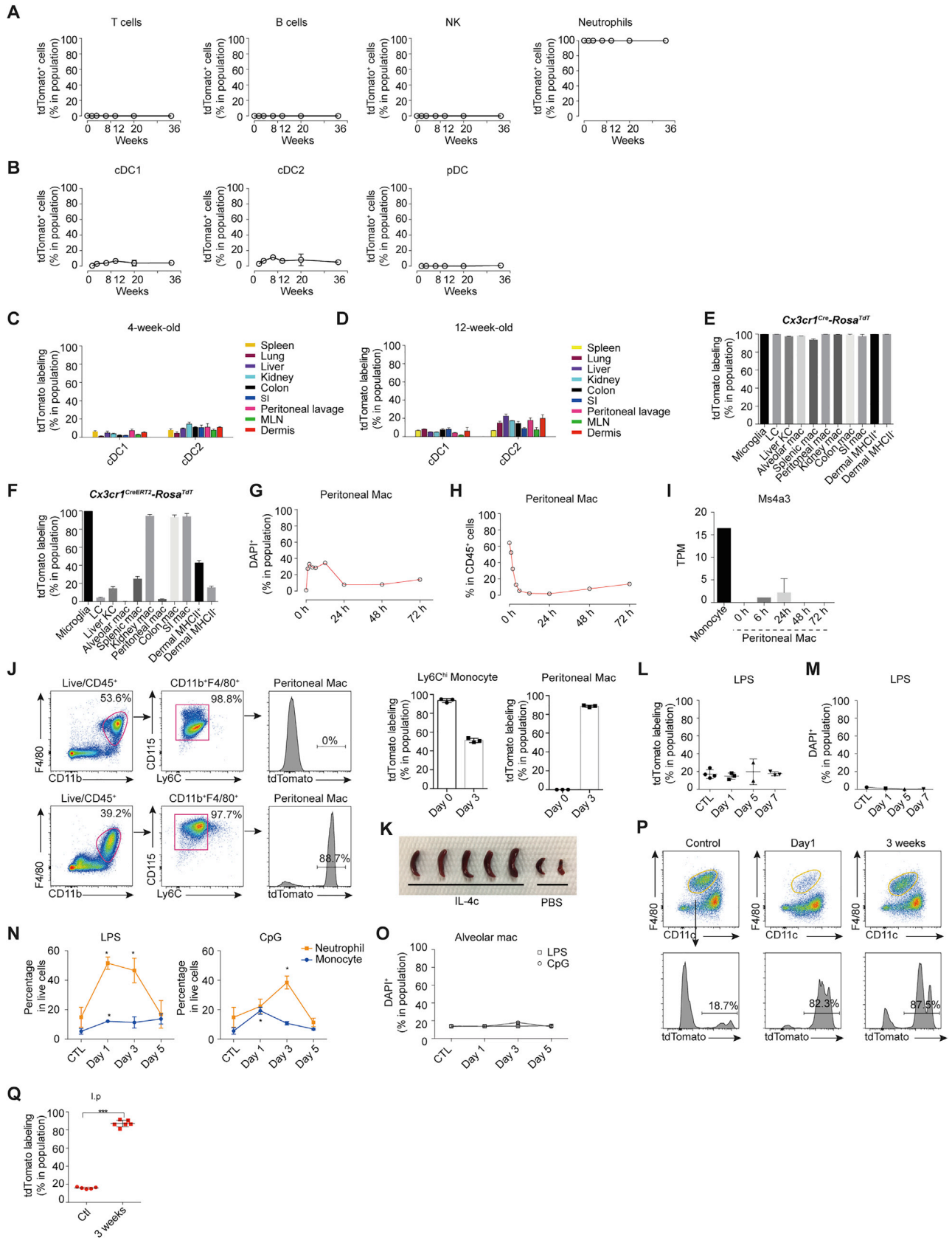
(A) Schematic of *Ms4a3*^{Cre} strategy. An *Ires-Cre* cassette was inserted after the stop codon. *Ms4a3*^{Cre} mice were crossed with *Rosa*^{tdTomato} reporter mice. In Cre-expressing cells, the *Stop* signal was irreversibly removed and tdTomato expression was induced. (B) Flow cytometric analysis of tdTomato expression in CD45⁺ tissue cells in *Ms4a3*^{Cre}-*Rosa*^{TdT} mice. Brain, epidermis, dermis, liver, lung, kidney, pancreas, heart, salivary gland, colon, small intestine and testis were analyzed. Experiments were repeated six times with 3-4 mice for each experiment. (C) Microscopic analysis showed dim tdTomato (red) expression in CD45⁺ cells in the testis of *Ms4a3*^{Cre}-*Rosa*^{TdT} mice. Cyan is CD45 and green is F4/80. (D) tdTomato expression in CD45⁺ cells in testis of *Ms4a3*^{TdT} reporter mice (filled gray) and WT mice (open black). (E) A *Cx3cr1*^{Cre}-based fate mapping model showed that Ly6C^{lo} monocytes are derived from Ly6C^{hi} monocytes (Yona et al., 2013); thus, labeling in Ly6C^{lo} monocytes should not be less than the labeling observed in Ly6C^{hi} monocytes. Our differential labeling pattern (95.1% versus 97.3%) suggested that Ly6C^{lo} monocytes could either be a heterogeneous population, with a minor tdTomato⁻ fraction not arising from the Ly6C^{hi} compartment, or that tdTomato⁻ cells contaminated the Ly6C^{lo} monocyte gate. To refine the gating of the Ly6C^{lo} population, we stained with the Ly6C^{lo} monocyte marker, CD43 (Ingersoll et al., 2010; Yanez et al., 2017): refining the Ly6C^{lo}CD43⁺ monocyte gate resulted in tdTomato Ly6C^{lo} monocyte labeling that was identical to Ly6C^{hi} monocyte labeling (97.3+/-0.30% versus 97.7+/-0.43%, respectively). tdTomato labeling in blood Ly6C^{hi}, Ly6C^{lo} and Ly6C^{lo}CD43⁺ populations in CD115⁺ monocytes, n = 9. (F) tSNE plot shows the labeling of tdTomato in peripheral blood, the color indicates the expression intensity of tdTomato, red indicates high expression, blue indicates low expression. (G) tdTomato labeling in different lymphoid and myeloid lineages of *Cx3cr1*^{Cre}-*Rosa*^{TdT} mice. The data are representative of 4 individual mice. The error bars represent SEM (H) Schematic of *Ms4a3*^{CreERT2} mice. An *Ires-CreERT2-pA* cassette was inserted after the stop codon. (I) Experimental protocol. Mice were injected with tamoxifen for 4 successive days, and analyzed on day 7. (J) tSNE plot shows the labeling of *Cx3cr1*-GFP in peripheral blood of *Cx3cr1*^{CreERT2}-*Rosa*^{TdT} mice, the color indicates the expression intensity of *Cx3cr1*, red indicates high expression, blue indicates low expression. (K) tdTomato labeling in different lymphoid and myeloid lineages of *Cx3cr1*^{CreERT2}-*Rosa*^{TdT} mice induced with tamoxifen. The data are representative of 4 individual mice. The error bars represent SEM.



(legend on next page)

Figure S6. MDPs Do Not Arise from GMPs *In Vitro* and *In Vivo*, Related to Figure 4

(A) Analysis of tdTomato⁺ BM cells. Plots show the distribution of tdTomato⁺ cells across different progenitor populations. (B) Analysis of tdTomato⁻ BM cells. Plots show the distribution of tdTomato⁻ cells across different progenitor populations. (C) Flow cytometric analysis of MDP defined by Fogg et al., the Ms4a3-tdTomato⁺ cells in the MDP gate were further analyzed with the gating strategy used by Hettinger et al. to define cMoPs. (D) Gating strategy used by Yanez et al.,. (E) Gating strategy used by Hettinger et al.,. (F) Production of DCs, monocytes, neutrophils and macrophages by indicated progenitors were analyzed by flow cytometry at day 4 of *in vitro* culture. (G) Production of DCs, monocytes and neutrophils by indicated progenitors were analyzed by flow cytometry at day 4 after adoptive transfer.



(legend on next page)

Figure S7. Monocyte Contribution to RTMs in Steady State and Inflammation, Related to Figure 6 and 7

(A) Kinetics of tdTomato labeling in lineages in peripheral blood. tdTomato labeling in T cells, B cells, NK cells and neutrophils from *Ms4a3^{Cre}-Rosa^{TdT}* mice was analyzed at different ages. n = 3-4 mice analyzed per time point. (B) Kinetics of tdTomato labeling in DCs in the spleen. tdTomato labeling in cDC1, cDC2 and pDCs from *Ms4a3^{Cre}-Rosa^{TdT}* mice was analyzed at different ages. n = 3-4 mice analyzed per time point. (C) tdTomato labeling of cDC1 and cDC2 in different organs from 4-week-old *Ms4a3^{Cre}-Rosa^{TdT}* mice. Experiments were repeated twice, and the data are representative of 4 mice. The error bars represent SEM (D) tdTomato labeling of cDC1 and cDC2 in different organs from 12-week-old *Ms4a3^{Cre}-Rosa^{TdT}* mice. Experiments were repeated twice, and the data are representative of 4 mice. The error bars represent SEM (E) tdTomato labeling in RTMs of *Cx3cr1^{Cre}-Rosa^{TdT}* mice, the data are representative of 4 individual mice. The error bars represent SEM (F) tdTomato labeling in RTMs of *Cx3cr1^{CreERT2}-Rosa^{TdT}* mice induced with 4 injections of tamoxifen and analyzed at day 7. The data are representative of 4 individual mice. The error bars represent SEM (G) DAPI⁺ relative numbers in peritoneal macrophages were analyzed at the indicated time points after i.p. thioglycollate injection. Results from one experiment with 3 mice per time point are shown. (H) Relative numbers of peritoneal macrophages in CD45⁺ cells were analyzed at the indicated time points after i.p. thioglycollate injection. Results from one experiment with 3 mice per time point are shown. (I) Peritoneal macrophages were sorted from thioglycollate treated mice at different time points and monocytes sorted from peritoneal lavage from 6 h time point, the expression of *Ms4a3* is shown, the y axis indicates TPMs of *Ms4a3* in each group. (J) *Ms4a3^{CreERT2}-Rosa^{TdT}* mice induced with 4 injections of tamoxifen and left for 3 days to washout tamoxifen, the mice were injected with thioglycollate (day 0) and analyzed on day 0 and day 3. tdTomato labeling in blood Ly6C^{hi} monocytes and peritoneal macrophages are shown, the data are representative of 4 individual mice. The error bars represent SEM (K) Images of spleen isolated from mice injected with IL-4c or PBS. (L) tdTomato labeling of peritoneal macrophages from *Ms4a3^{Cre}-Rosa^{TdT}* mice injected with LPS was analyzed at the indicated time points. (M) DAPI⁺ relative numbers in peritoneal macrophages were analyzed at the indicated time points after i.p. administration of LPS. Results from one experiment with 3 mice per time point are shown. (N) Relative numbers of neutrophils (yellow) and monocytes (blue) in live cells of the lung. Results from one experiment with three mice per time point. (O) DAPI⁺ relative numbers in AMs were analyzed at the indicated time points after i.n. administration of CpG or LPS. Results from one experiment with three mice per time point are shown. (P) Flow cytometric analysis of splenic macrophages from *Ms4a3^{Cre}-Rosa^{TdT}* mice at the indicated time points after i.p. injection of 200 μ L clodronate liposome and (Q) tdTomato labeling in splenic macrophages from *Ms4a3^{Cre}-Rosa^{TdT}* after macrophage depletion by clodronate liposome i.p. injection, n = 5-6 for each group. Statistical significance is indicated by ***p < 0.001. The error bars represent SEM.